NASA Technical Memorandum 104566, Vol. 27

SeaWiFS Technical Report Series

Stanford B. Hooker, Editor
Goddard Space Flight Center
Greenbelt, Maryland

James G. Acker, Technical Editor
Hughes STX
Lanham, Maryland

Elaine R. Firestone, Technical Editor
General Sciences Corporation
Laurel, Maryland

Volume 27, Case Studies for SeaWiFS Calibration and Validation, Part 3

J. L. Mueller
San Diego State University
San Diego, California

R. A. Barnes
ManTech Environmental Technology, Inc.
Wallops Island, Virginia

R. S. Fraser
NASA Goddard Space Flight Center
Greenbelt, Maryland

C. T. Weir, D. A. Seigel, and D. W. Menzies
University of California at Santa Barbara
Santa Barbara, California

S. F. Biggar, K. J. Thome, and P. N. Slater
University of Arizona
Tucson, Arizona

A. F. Michaels
Bermuda Biological Station for Research
Ferry Reach, Bermuda

A. W. Holmes
Santa Barbara Research Center
Goleta, California

G. Podesta
University of Miami
Miami, Florida

National Aeronautics and
Space Administration

Goddard Space Flight Center
Greenbelt, Maryland 20771

1995

This publication is available from the NASA Center for AeroSpace Information,
800 Elkridge Landing Road, Linthicum Heights, MD 21090-2934, (301) 621-0390.

PREFACE

The scope of the Sea-viewing Wide Field-of-view Sensor (SeaWiFS) Calibration and Validation Program encompasses a broad variety of topics, as evidenced by the contents of two previous *case studies* volumes in the *SeaWiFS Technical Report Series*—Volumes 13 and 19. Each case studies volume contains several chapters discussing topics germane to the Calibration and Validation Program. Volume 27, the third collection of case studies, further demonstrates both the breadth and complexity of the issues that the Program must address, and provides further justification for a comprehensive calibration and validation effort.

The chapters in this volume present discussions of:

a) Results on the measurement of immersion coefficients for submersible radiometers;

b) The effect of oxygen absorption on the 765 nm SeaWiFS channel;

c) The results of the second SeaWiFS ground-based solar calibration experiment, which was performed *after* the instrument was modified to reduce internal stray light;

d) Ship shadow effects on subsurface radiance and irradiance measurements; and

e) The definition of the SeaWiFS data day for level-3 data binning.

Greenbelt, Maryland
January 1995

—C. R. McClain

Table of Contents

Prologue 1
1. Comparison of Irradiance Immersion Coefficients for Several Marine Environmental Radiometers (MERs) 3
1.1 Introduction 3
1.2 Method and Results 3
1.3 Discussion 4
2. The Effect of Oxygen Absorption on Band-7 Radiance 16
2.1 Introduction 16
2.2 Theory 16
2.3 Conclusion 19
3. Second SeaWiFS Preflight Solar Radiation-Based Calibration Experiment 20
3.1 Introduction 20
3.2 Experimental Method 20
3.3 Results 21
3.4 Discussion 24
4. *In Situ* Evaluation of a Ship's Shadow 25
4.1 Introduction 25
4.2 Experimental Methods 26
4.3 Results 27
4.3.1 Simultaneous Comparison 27
4.3.2 Multi-Distance Comparison 28
4.4 Discussion 28
5. SeaWiFS Global Fields: What's In a Day? 34
5.1 Introduction 34
5.2 Temporal Definition 34
5.3 Spatial Definition 35
5.3.1 Beginning of the Data Day 36
5.3.2 Advantages of the Spatial Definition 38
5.3.3 An Alternative Explanation 40
5.4 Other Issues 42
GLOSSARY 43
SYMBOLS 43
REFERENCES 44
THE SEAWIFS TECHNICAL REPORT SERIES 45

ABSTRACT

This document provides brief reports, or case studies, on a number of investigations sponsored by the Calibration and Validation Team (CVT) within the Sea-viewing Wide Field-of-view Sensor (SeaWiFS) Project. Chapter 1 describes a comparison of the irradiance immersion coefficients determined for several different marine environmental radiometers (MERs). Chapter 2 presents an analysis of how light absorption by atmospheric oxygen will influence the radiance measurements in band 7 of the SeaWiFS instrument. Chapter 3 gives the results of the second ground-based solar calibration of the instrument, which was undertaken after the sensor was modified to reduce the effects of internal stray light. (The first ground-based solar calibration of SeaWiFS is described in Volume 19 in the *SeaWiFS Technical Report Series.*) Chapter 4 evaluates the effects of ship shadow on subsurface irradiance and radiance measurements deployed from the deck of the R/V *Weatherbird II* in the Atlantic Ocean near Bermuda. Chapter 5 illustrates the various ways in which a single *data day* of SeaWiFS observations can be defined, and why the spatial definition is superior to the temporal definition for operational usage.

Prologue

The purposes of the Sea-viewing Wide Field-of-view Sensor (SeaWiFS) Project is to obtain valid ocean color data of the world ocean for a five-year period, to process that data in conjunction with ancillary data to meaningful biological parameters, and to make that data readily available to researchers. The National Aeronautics and Space Administration (NASA) Goddard Space Flight Center (GSFC) will develop a data processing and archiving system in conjunction with the Earth Observing System Data and Information System (EOSDIS), which includes a ground receiving system; EOSDIS will oversee a calibration and validation effort which is designed to ensure the integrity of the final products.

The Calibration and Validation Team (CVT) has three main tasks:

1) Calibration of the SeaWiFS instrument;
2) Development and validation of the operational atmospheric correction algorithm; and
3) Development and validation of the derived product algorithms, such as chlorophyll *a* concentration.

Some of this work will be done internally at GSFC, while the remainder will be done externally at other institutions. NASA and the Project place the highest priority on assuring the accuracy of derived water-leaving radiances globally, and over the duration of the entire mission. If these criteria are met, the development of global and regional biogeochemical algorithms can proceed on many fronts. These various activities are discussed in detail in *The SeaWiFS Calibration and Validation Plan* (McClain et al. 1992).

Because many of the studies and other works undertaken with the Calibration and Validation Program are not extensive enough to require dedicated volumes of the *SeaWiFS Technical Report Series*, the CVT has decided to publish volumes composed of brief, but topically specific, chapters. Volume 13 was the first volume, and consists primarily of contributions related to atmospheric correction methodologies, ancillary data sets required for level-2 processing of Coastal Zone Color Scanner (CZCS) and SeaWiFS data, laboratory techniques for instrument calibration relevant to calibration round-robins, and field observations designed for transferring the prelaunch calibration to orbit, and in interpreting the on-orbit lunar calibration data. The second case studies volume, Volume 19, contains chapters on atmospheric and glint corrections, solar-, lunar-, and integrating sphere optical measurements, data format considerations, and the use of ancillary data (including surface wind velocities) in SeaWiFS processing. Volume 26 is the third in the set of such volumes. A short synopsis of each chapter in this volume is given below.

1. Comparison of Irradiance Immersion Coefficients for Several Marine Environmental Radiometers (MERs)

This chapter describes how spectral immersion coefficients were measured experimentally for 12 irradiance collectors on underwater profiling radiometers. These coefficients are used to convert spectral radiance responsivity calibration factors, measured in air, for use underwater. At any given wavelength, the immersion coefficients typically had standard deviations between collectors ranging from 3–5%. The total variations at some wavelengths were as large as 10%. Repeated measurements on several of the collectors showed that experimental uncertainty is not greater than 1%. The primary conclusion of this study is that accurate underwater radiometry *absolutely* requires experimental characterization of each individual irradiance collector, rather than assuming a value based solely on its design and material specifications.

2. *The Effect of Oxygen Absorption on Band-7 Radiance*

Atmospheric oxygen absorbs about 13% of the available sunlight reflected from the Earth in band 7 of the SeaWiFS instrument. If a correction is made for the average amount of absorption, then the measured radiance would vary by ± 0.004 for a two standard deviation (2σ) variability in the amount of oxygen in a vertical column. For comparison, the instrumental noise is about one-half, or 0.002, of this variation. A correction based on the regional changes in absorption as a function of season would not significantly reduce the statistical variation in absorption.

3. *Second SeaWiFS Preflight Solar Radiation-Based Calibration Experiment*

This paper describes the second solar radiation-based calibration of SeaWiFS. The experiment was done on 1 November 1993 in the rock garden at the Santa Barbara Research Center (SBRC). The results of the calibration are presented, along with a comparison to the spherical integrating source (SIS) calibration done at SBRC. The estimated uncertainty of the SIS calibration is 2.8%, compared to the 4% estimated uncertainty for the solar-based calibration. There is also an uncertainty in the value of the exoatmospheric solar irradiance used to make this comparison, which is probably on the order of 1%. In addition, the integrated out-of-band blocking for SeaWiFS is in the 1–3% range, which can introduce significant differences between the lamp- and solar-based calibrations. This agreement is better than anticipated, and better than the agreement achieved in March 1993 from the first experiment. The better agreement is probably due to a sphere recalibration between the two experiments.

4. *In Situ Evaluation of a Ship's Shadow*

In situ measurements of optical properties made from a ship can be biased by the ship's shadow. In an effort to evaluate the ship shadow perturbation created by the R/V *Weatherbird II,* profiles of downwelling irradiance, $E_d(z,\lambda)$; upwelling radiance, $L_u(z,\lambda)$; and derived apparent optical properties (AOPs), were obtained at four distances—1 m, 3 m, 6 m, and 20 m or more—off the ship's stern. Two statistical analyses of these data are explored. The first analysis uses data from pairs of simultaneously-obtained light profiles, one profile obtained at a distance greater than 20 m from the stern of the ship, and the other taken either 1 or 6 m off the stern. The second analysis compares the derived AOPs for each profiling distance from the ship, using data obtained throughout the length of the experiment. Significant differences are rare in comparisons of profiles obtained at least 3 m off the ship's stern. At 1 m off the stern, however, significant discrepancies are intermittently observed. This work illustrates that the inherent sources of noise in determining radiative fluxes and AOPs in the upper ocean are generally greater than the effects incurred by the ship's own shadow under optimal conditions.

5. *SeaWiFS Global Fields: What's In a Day?*

This chapter defines the procedure to be employed to delineate data corresponding to *one day* of SeaWiFS operation. The definition is required for data analysis with minimal temporal aliasing in the same region of observation. The definition also allows proper assignment of data into daily fields that will be used for the generation of weekly and monthly average products.

Chapter 1

Comparison of Irradiance Immersion Coefficients for Several Marine Environmental Radiometers (MERs)

JAMES L. MUELLER
San Diego State University
San Diego, California

ABSTRACT

Spectral immersion coefficients were measured experimentally for 12 irradiance collectors on underwater profiling radiometers. These coefficients are used to convert spectral irradiance responsivity calibration factors, measured in air, for use underwater. All of the irradiance collectors were the same design, however, 11 were made of Plexiglas® diffusing material and 1 was made of Teflon®. At any given wavelength, the immersion coefficients typically had standard deviations between collectors ranging from 3–5%. The total variations at some wavelengths were as large as 10%. The coefficients of the Teflon diffuser were well within the bounds of one standard deviation from the sample mean. Repeated measurements on several of the collectors showed that experimental uncertainty is not greater than 1% (one standard deviation, or 1σ). The primary conclusion of this study is that accurate underwater radiometry *absolutely* requires experimental characterization of each individual irradiance collector, rather than assuming a value based solely on its design and material specifications.

1.1 INTRODUCTION

The spectral responsivities of underwater (irradiance) radiometers are calibrated in air using an FEL lamp, which has a spectral irradiance scale traceable to the National Institute of Standards and Technology (NIST). The spectral immersion coefficients for an underwater irradiance meter represent the differences between the instrument's spectral responsivities in air and in water. The responsivity will change due to the fact that the refractive index of the plastic (or Teflon®) diffuser is smaller, relative to the refractive index of water, than it is relative to the refractive index of air. Less incident light is reflected at the water-plastic interface, and therefore, more of the light reflected from the collector's inner surface escapes back into the water. The net result is that a smaller fraction of incident flux is transmitted through the irradiance collector in water and therefore, the instrument's irradiance responsivity is decreased.

At present, the practice of the oceanographic community is to experimentally characterize the spectral immersion coefficients of only a small sample of irradiance collectors in a given class of collectors (with the same materials and design specifications). These coefficients have subsequently been associated with *all* collectors in that class, which assumes negligible variability between individual items. In a previous report (Mueller 1994), this assumption was tested by comparing irradiance immersion coefficients for several MER-series radiometers manufactured by Biospherical Instruments, Inc. (BSI) of San Diego, California. The results of that preliminary comparison between measured spectral immersion coefficients for six Plexiglas® diffusers of the same material and design specifications show significant variations, with standard deviations (σ) ranging from 3.2–3.5% and ranges (maximum minus minimum) as large as 9%. In this earlier work, however, the immersion tests on each instrument were not replicated, and thus, no estimates of the experimental uncertainty of the measurements could be made. The conclusions were, therefore, only tentative.

This report presents results of an extended series of immersion characterization experiments on an expanded sample of irradiance collectors. The new series of characterization experiments were repeated two or more times, at different lamp-to-collector distances, to provide an estimate of the uncertainty in this laboratory's experimental determinations of immersion coefficients. The new results were then pooled with the earlier sample (Mueller 1994) to analyze overall variability between individual collectors.

1.2 METHOD AND RESULTS

The laboratory procedure for determining an irradiance meter's spectral immersion coefficients is described in

Mueller and Austin (1992). Immersion coefficients taken from Mueller (1994) were each based on a single experimental measurement. Subsequently, a new set of experimental measurements were repeated 2–4 times on each of seven irradiance collectors as a basis for uncertainty estimates. In each case, the immersion test (Mueller and Austin 1992) was done first at one lamp-to-collector distance, and then the lamp was moved 12.5 cm toward the collector and the test was repeated. In addition, the entire procedure was repeated on different days for four of the collectors, and for a fifth instrument [MER-1012f, Serial Number (S/N) 8107] the single day results from this laboratory were combined with the results of an independent immersion characterization by BSI.

Table 1. Immersion coefficients for several MERs characterized at CHORS. The column headings denote the MER model number and irradiance type. The data is extracted from Mueller (1994).

Wavelength [nm]	*MER-1048*†		*MER-2040*‡	
	E_d	E_u	E_d	E_u
408	1.3686			
410		1.4315	1.3882	1.3019
439	1.4289			
440		1.4456		
441			1.3846	1.3212
465			1.3751	1.3158
488	1.4138		1.3591	1.3012
489		1.4169		
518	1.3841			
519		1.3952		
520			1.3470	1.2865
548		1.3822		
550	1.3704			
560	1.3693		1.3265	1.2695
589	1.3654	1.3699	1.3088	1.2557
632	1.3339			
655	1.3425		1.2804	1.2332
671	1.3236	1.3344		
683	1.3997			
693	1.3724	1.3233		
709	1.3389			

† MER S/N 8302. ‡ MER S/N 8716.

Table 1 lists spectral irradiance immersion coefficients for two MER instruments (i.e., four irradiance collectors) characterized at the San Diego State University (SDSU) Center for Hydro-Optics and Remote Sensing (CHORS) during 1993 (Mueller 1994). Immersion coefficients for seven additional collectors are listed in Tables 2–8, together with mean, standard deviation, and range for replicated tests at each wavelength. Spectral immersion coefficients from all collectors are illustrated in Fig. 1 (which includes all data from Table 1, and mean coefficients from Tables 2–8). Coefficients from replicate experiments, and the experimental mean values, for each individual collector (Tables 2–8) are illustrated in Figs. 2–8, respectively.

Linear regression analyses provide a reasonable fit for many of the instrumental immersion coefficients, F_i, to an equation of the form

$$F_i = a - \frac{b\lambda}{10^4} \quad (1)$$

where λ is the wavelength in nanometers. Regression coefficients a and b; residual standard deviations, s_{xy}; and squared linear correlation coefficients, R^2; are compared for these instruments in Table 9, and the regression lines are illustrated in Figs. 2 and 4–8.

Mean, range, and σ of immersion coefficients for subsamples of different collectors were computed at selected wavelengths and are presented in Table 10.

1.3 DISCUSSION

This report compares the experimentally determined immersion coefficients for the irradiance collectors on nine MER-series underwater radiometers manufactured by BSI. There are 12 irradiance collectors involved in these experiments, all having the same basic design—11 have Plexiglas diffusers and 1 (MER-2040 S/N 8738) has a Teflon diffusers (Table 8 and Fig. 8).

The replicated experiments summarized in Tables 2–8 show that, for the majority of channels tested, the 1σ uncertainties in experimentally determined immersion coefficients are approximately 1% or less. The notable exceptions are the $E_d(\lambda)$ channels at wavelengths greater than 550 nm of the MER-1012f S/N 8107 (Fig. 2 and Table 2) and MER-1015 S/N 8205 (Fig. 3 and Table 3). It is suspected that these larger uncertainties may indicate nonlinearities in the responsivities of these channels. Nonlinearity may be due to a voltage discontinuity across a gain change in replicated experiments at different lamp-to-collector distances.

The total range between the immersion coefficients of the 12 collectors is as large as 15% at some wavelengths (Fig. 1 and Table 10). The standard deviation of dispersion in immersion coefficients is generally between 3.5–5%, at least at those wavelengths for which collector sample sizes were large enough to estimate a reasonable standard deviation (Table 10).

Immersion coefficients vary linearly with wavelength for many of the diffusers (Table 9, and Figs. 2 and 4–8), with residual standard deviation $s_{xy} \times 100\% \leq 1\%$ (except for the MER-2040 S/N 8725, where $s_{xy} \times 100\% = 1.7\%$). The immersion coefficients for the MER-1015 S/N 8205 are not a well-behaved linear function of wavelength.

The dispersion in immersion coefficients between these irradiance collectors (Fig. 1 and Table 10) is too large to neglect, and the results of the replicated experiments indicate that only a small fraction of this variation can be

Table 2. Immersion coefficients measured experimentally for the MER-1012f (S/N 8107). The data are presented here in order of decreasing lamp-to-collector distance.

Wavelength [nm]	*24 June 1994* 144.5 cm	*24 June 1994* 130.0 cm	*17 March 1994*† 106.3 cm	*Immersion Coefficient* μ	σ	*Range*
406.9	1.3510	1.3492	1.3512	1.3505	0.0009	0.0020
442.5	1.3673	1.3643	1.3685	1.3667	0.0018	0.0042
487.1	1.3499	1.3454	1.3501	1.3485	0.0022	0.0048
517.8	1.3383	1.3344	1.3391	1.3373	0.0020	0.0047
564.9	1.3178	1.3388	1.3195	1.3254	0.0095	0.0210
632.3	1.3130	1.2961	1.3246	1.3112	0.0117	0.0286
681.3	1.3044	1.2636	1.2807	1.2829	0.0167	0.0408

† Immersion coefficients calculated from experimental measurements by BSI.

Table 3. Immersion coefficients measured experimentally for the MER-1015 (S/N 8205).

Wavelength [nm]	*1 September 1994* 152.2 cm	137.8 cm	*2 September 1994* 152.2 cm	137.8 cm	*Immersion Coefficient* μ	σ	*Range*
406.0	1.4159	1.4217	1.4233	1.4104	1.4178	0.0051	0.0130
438.5	1.4335	1.4473	1.4351	1.4398	1.4389	0.0054	0.0138
462.4	1.4253	1.4371	1.4309	1.4291	1.4306	0.0043	0.0118
485.5	1.4210	1.4248	1.4227	1.4177	1.4215	0.0026	0.0071
517.9	1.4031	1.4083	1.4071	1.4022	1.4052	0.0026	0.0060
536.8	1.3929	1.4004	1.3965	1.3930	1.3957	0.0031	0.0075
558.5	1.3843	1.3196	1.3879	1.3183	1.3525	0.0336	0.0696
588.4	1.3104	1.4189	1.3169	1.4171	1.3658	0.0522	0.1086
624.2	1.4494	1.4065	1.4448	1.3955	1.4240	0.0235	0.0539
673.3	1.4325	1.3993	1.4482	1.3861	1.4165	0.0249	0.0621
696.2	1.3846	1.3507	1.3730	1.3418	1.3625	0.0171	0.0428
762.4	1.3120	1.3131	1.3151	1.3109	1.3128	0.0016	0.0042

Table 4. Immersion coefficients measured experimentally for the MER-1032 (S/N 8301). The data are presented here to allow comparison for similar lamp-to-collector distances.

Wavelength [nm]	*30 December 1993* 120.0 cm	*22 July 1992* 138.0 cm	123.5 cm	*26 July 1992* 137.9 cm	123.5 cm	*Immersion Coefficient* μ	σ	*Range*
411.1	1.4053	1.4172	1.4136	1.4112	1.4037	1.4102	0.0057	0.0135
441.9	1.3946	1.4302	1.4016	1.4146	1.4005	1.4083	0.0143	0.0356
452.9	1.3897	1.4091	1.4129	1.4089	1.4096	1.4060	0.0093	0.0232
489.6	1.3754	1.3887	1.3918	1.3945	1.3925	1.3886	0.0077	0.0191
508.9	1.3795	1.3877	1.3854	1.3889	1.3819	1.3847	0.0039	0.0094
528.6	1.3529	1.3790	1.3753	1.3795	1.3735	1.3720	0.0110	0.0266
555.3	1.3451	1.3664	1.3618	1.3679	1.3622	1.3607	0.0091	0.0229
588.9	1.3329	1.3540	1.3450	1.3577	1.3490	1.3477	0.0096	0.0248
632.1	1.3071	1.3337	1.3271	1.3348	1.3280	1.3261	0.0112	0.0276
654.8	1.3013	1.3222	1.3153	1.3184	1.3151	1.3145	0.0079	0.0209
670.7	1.3032	1.3285	1.3232	1.3279	1.3219	1.3209	0.0103	0.0253

Table 5. Immersion coefficients measured experimentally for the MER-1032 (S/N 8301).

Wavelength	*22 July 1994*		*26 July 1994*		*Immersion Coefficient*		
[nm]	131.6 cm	123.5 cm	131.6 cm	117.2 cm	μ	σ	*Range*
411.3	1.4532	1.4508	1.4458	1.4427	1.4481	0.0041	0.0105
442.0	1.4216	1.4214	1.4165	1.4156	1.4188	0.0027	0.0060
489.9	1.3999	1.4017	1.3987	1.3961	1.3991	0.0020	0.0056
509.1	1.3859	1.3877	1.3845	1.3819	1.3850	0.0021	0.0058
555.4	1.3664	1.3658	1.3664	1.3595	1.3645	0.0029	0.0069
529.1	1.3788	1.3783	1.3773	1.3735	1.3770	0.0021	0.0053
633.0	1.3108	1.3271	1.3103	1.3204	1.3172	0.0070	0.0168
670.9	1.3237	1.3113	1.3249	1.3068	1.3167	0.0078	0.0181

Table 6. Immersion coefficients measured experimentally for the MER-2040 (S/N 8724).

Wavelength	*22 July 1994*		*26 July 1994*		*Immersion Coefficient*		
[nm]	121.6 cm	107.2 cm	121.6 cm	107.2 cm	μ	σ	*Range*
453.2	1.4086	1.4077	1.4116	1.4117	1.4099	0.0018	0.0040
440.3	1.4144	1.4143	1.4186	1.4187	1.4165	0.0021	0.0044
486.7	1.3942	1.3931	1.3987	1.3980	1.3960	0.0024	0.0056
516.9	1.3783	1.3825	1.3828	1.3870	1.3827	0.0031	0.0087
530.2	1.3724	1.3762	1.3770	1.3807	1.3766	0.0029	0.0083
565.1	1.3560	1.3554	1.3604	1.3602	1.3580	0.0023	0.0050
664.0	1.3175	1.3167	1.3218	1.3213	1.3193	0.0022	0.0050

Table 7. Immersion coefficients measured experimentally for the MER-2040 (S/N 8725).

Wavelength	*2 September 1994*		*Immersion Coefficient*		
[nm]	125.4 cm	111.0 cm	μ	σ	*Range*
408.6	1.3150	1.3177	1.3164	0.0014	0.0028
438.9	1.3451	1.3380	1.3415	0.0035	0.0071
484.9	1.3449	1.3394	1.3421	0.0028	0.0056
617.6	1.3366	1.3398	1.3382	0.0016	0.0032
564.0	1.3223	1.3206	1.3215	0.0008	0.0016
662.6	1.3011	1.2997	1.3004	0.0007	0.0014

Table 8. Immersion coefficients measured experimentally for the MER-2040 (S/N 8738).

Wavelength	*24 June 1994*	*29 June 1994*	*Immersion Coefficient*		
[nm]	120.7 cm	106.2 cm	μ	σ	*Range*
340.0	1.4281	1.4170	1.4225	0.0055	0.0111
380.0	1.4127	1.4033	1.4080	0.0047	0.0094
412.0	1.3996	1.3917	1.3956	0.0039	0.0079
443.0	1.3870	1.3804	1.3837	0.0033	0.0066
395.0	1.4053	1.3977	1.4015	0.0038	0.0076
665.0	1.3126	1.3078	1.3102	0.0024	0.0047
455.0	1.3835	1.3772	1.3803	0.0032	0.0064
490.0	1.3714	1.3652	1.3683	0.0031	0.0062
510.0	1.3638	1.3580	1.3609	0.0029	0.0058
532.0	1.3570	1.3467	1.3518	0.0052	0.0103
555.0	1.3486	1.3380	1.3433	0.0053	0.0106
570.0	1.3447	1.3325	1.3386	0.0061	0.0122

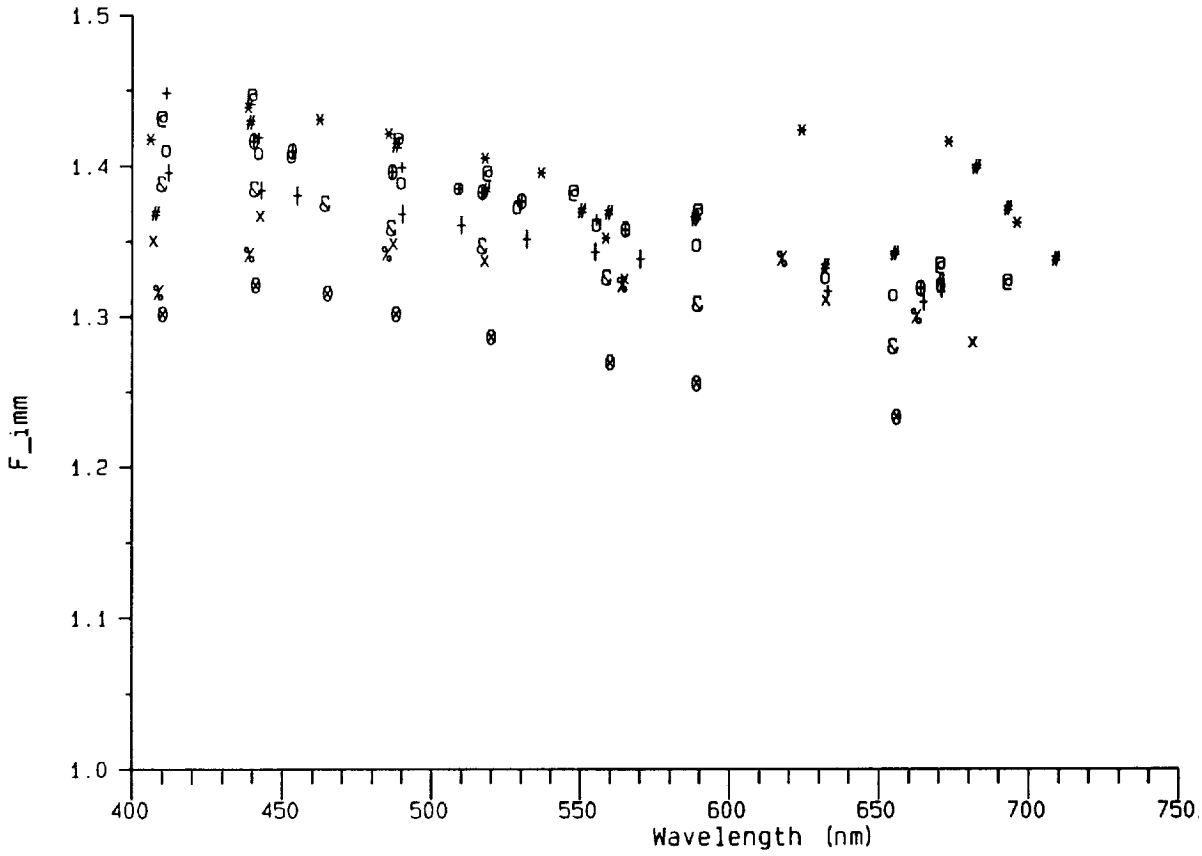

Fig. 1. Immersion coefficients (F_i) for several MER-series radiometers.

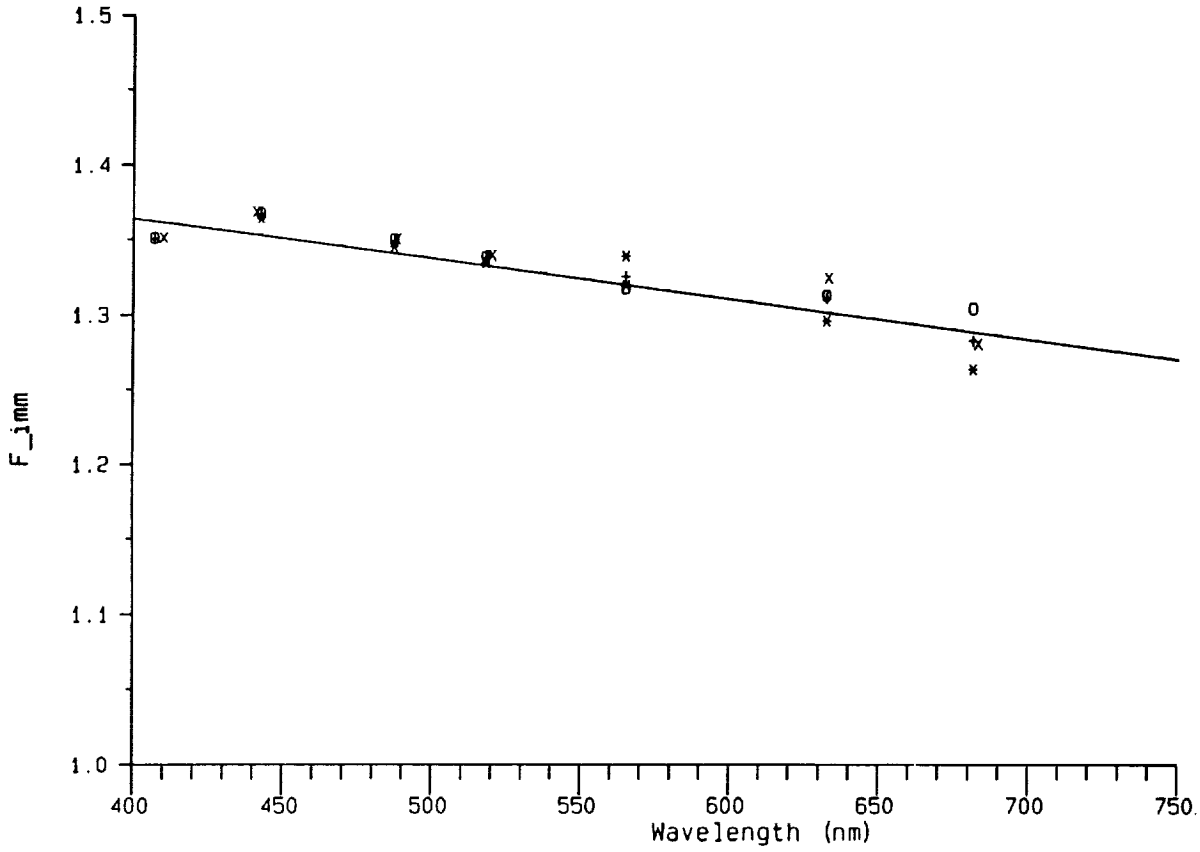

Fig. 2. Immersion coefficients from replicate immersion tests on the MER-1012f (S/N 8107) E_d channels. The legend in the figure provides experiment dates and lamp-to-collector distances. The solid line is the least-squares regression fit to the mean coefficients.

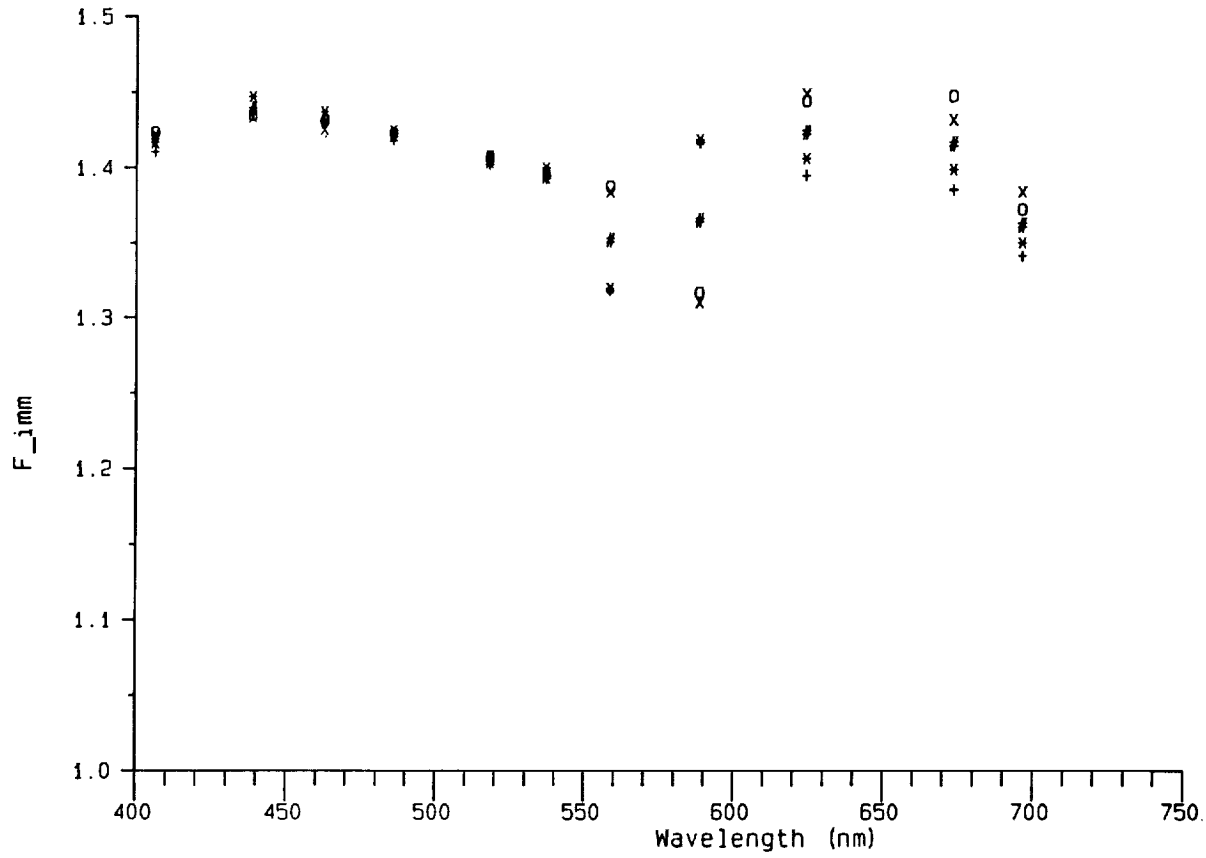

9/1/94, R = 152.2 cm: x
9/1/94, R = 137.8 cm: *
9/2/94, R = 152.2 cm: o
9/2/94, R = 137.8 cm: +
MEAN: #

Fig. 3. Immersion coefficients from replicate immersion tests on the MER-1015 (S/N 8205) E_d channels. The legend in the figure provides experiment dates and lamp-to-collector distances.

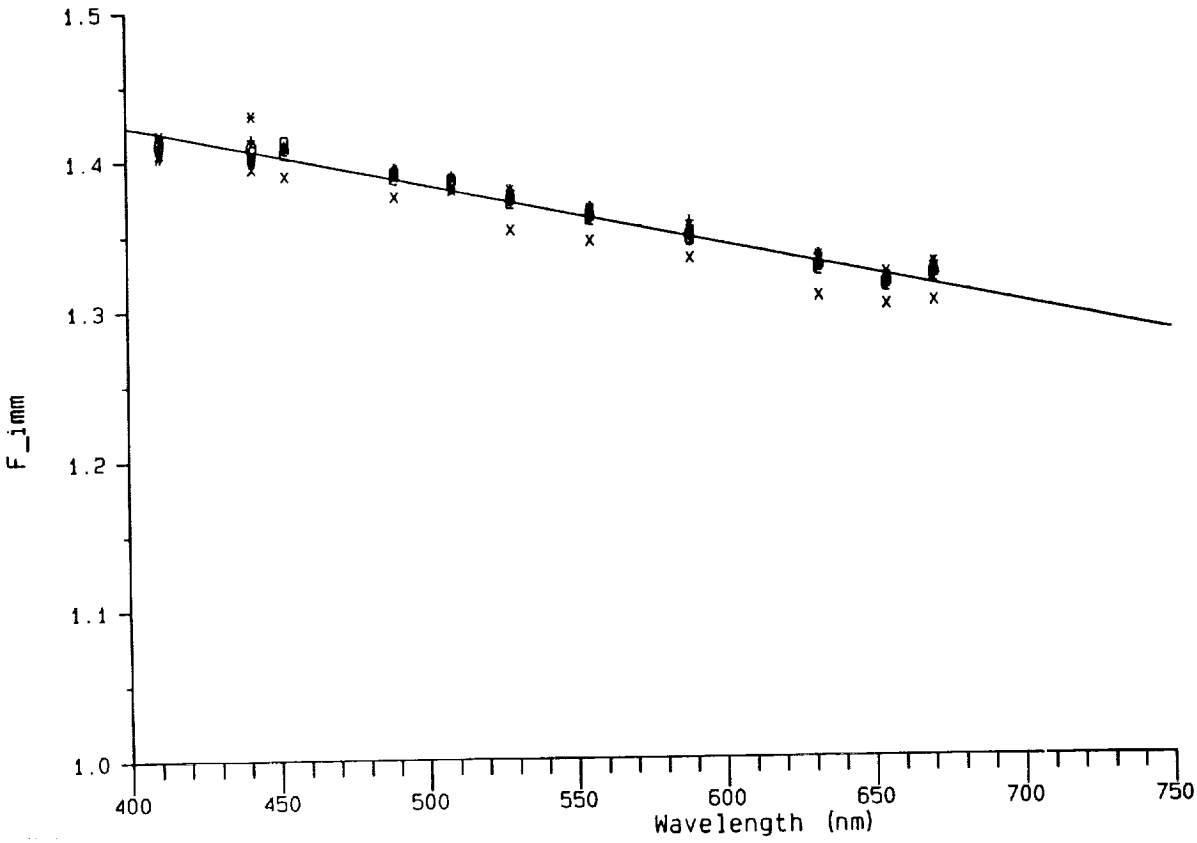

Fig. 4. Immersion coefficients from replicate immersion tests on the MER-1032 (S/N 8301) E_d channels. The legend in the figure provides experiment dates and lamp-to-collector distances. The solid line is the least-squares regression fit to the mean coefficients.

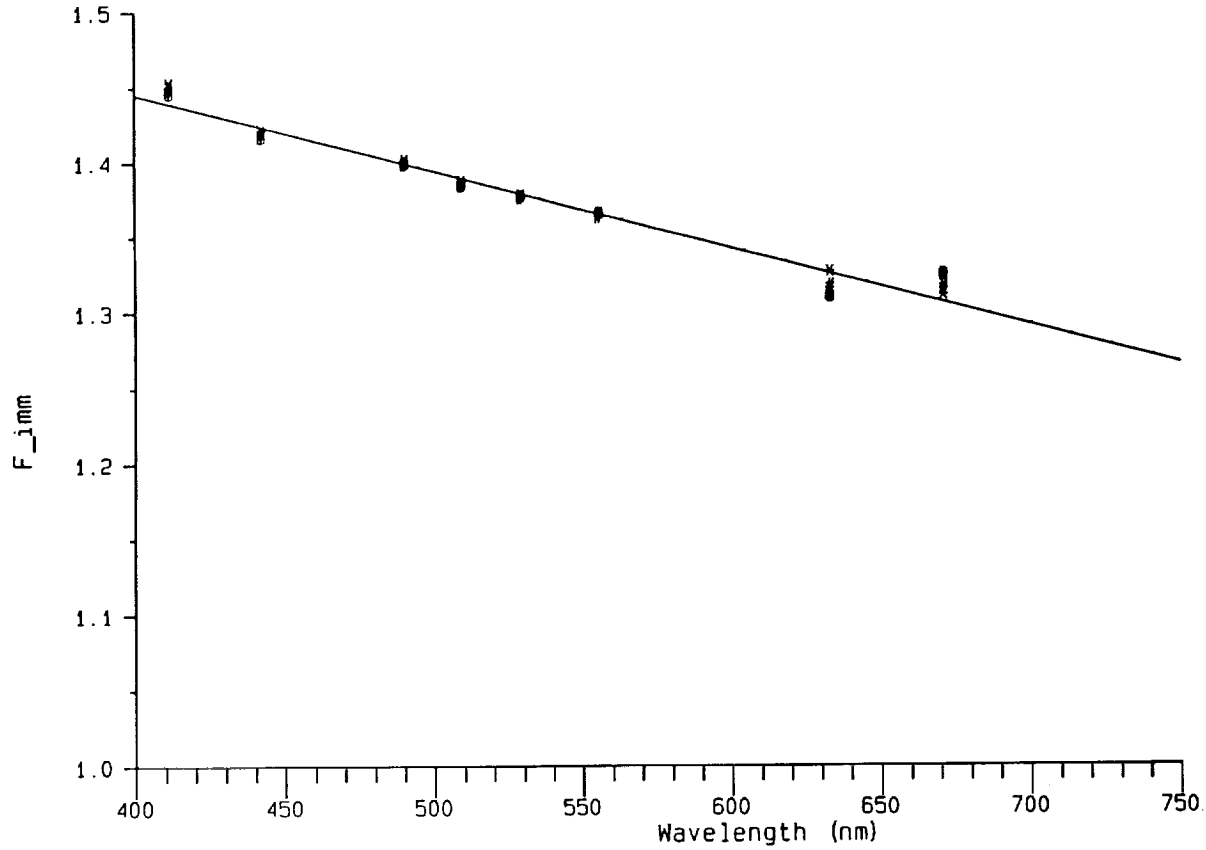

Fig. 5. Immersion coefficients from replicate immersion tests on the MER-1032 (S/N 8301) E_u channels. The legend in the figure provides experiment dates and lamp-to-collector distances. The solid line is the least-squares regression fit to the mean coefficients.

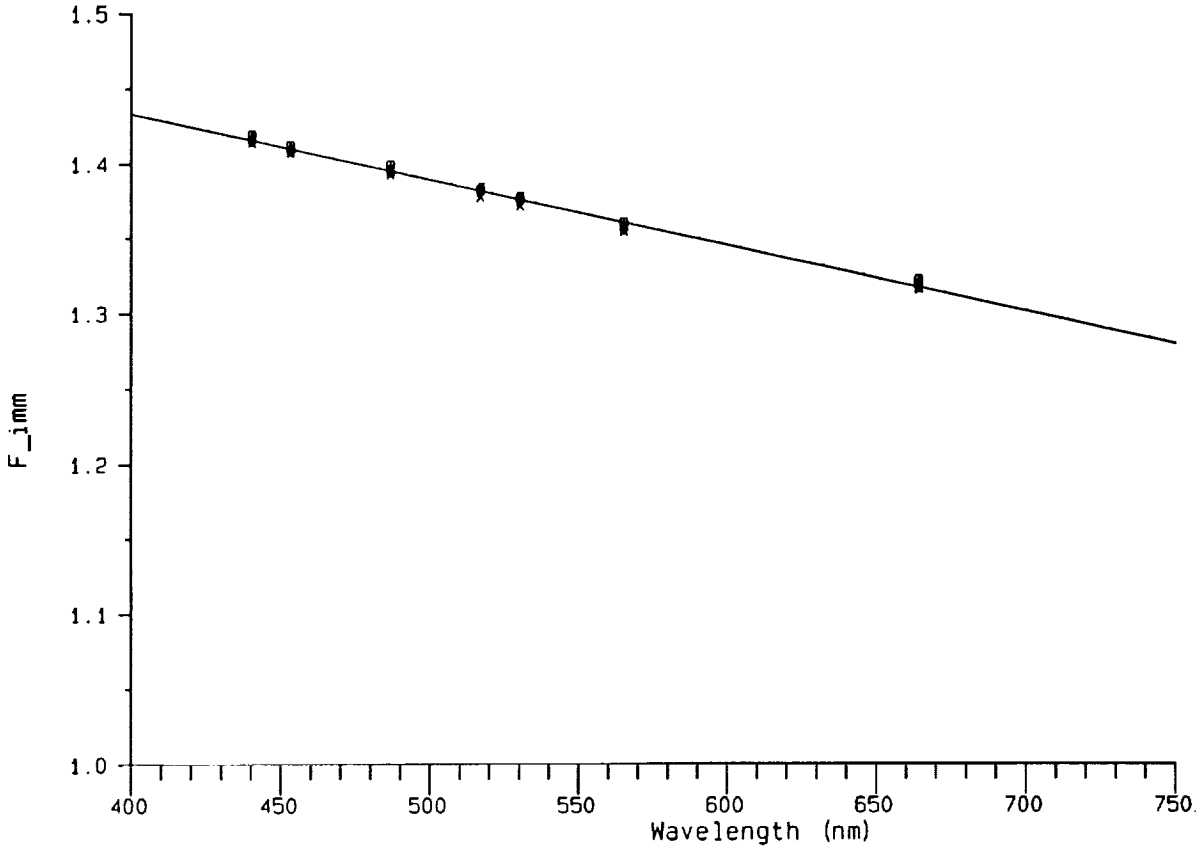

Fig. 6. Immersion coefficients from replicate immersion tests on the MER-2040 (S/N 8724) E_d channels. The legend in the figure provides experiment dates and lamp-to-collector distances. The solid line is the least-squares regression fit to the mean coefficients.

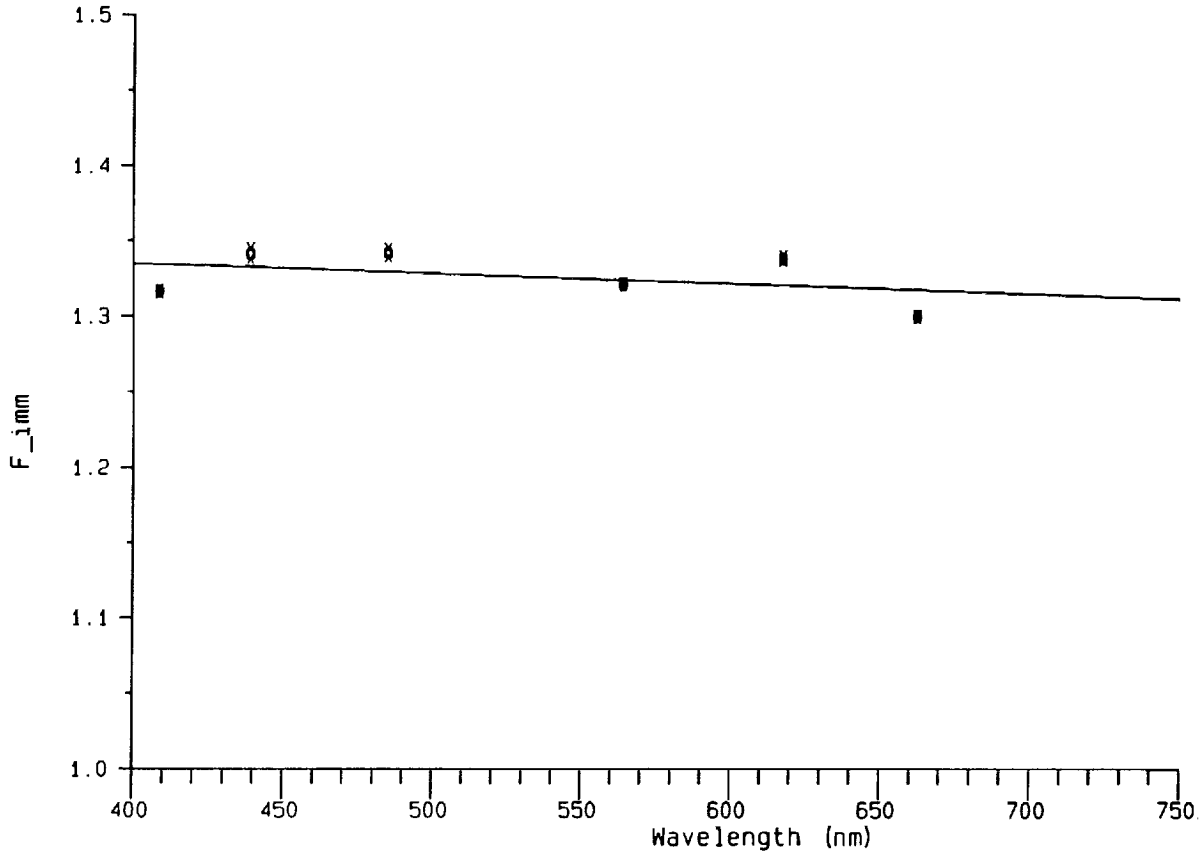

Fig. 7. Immersion coefficients from replicate immersion tests on the MER-2040 (S/N 8725) E_d channels. The legend in the figure provides experiment dates and lamp-to-collector distances. The solid line is the least-squares regression fit to the mean coefficients.

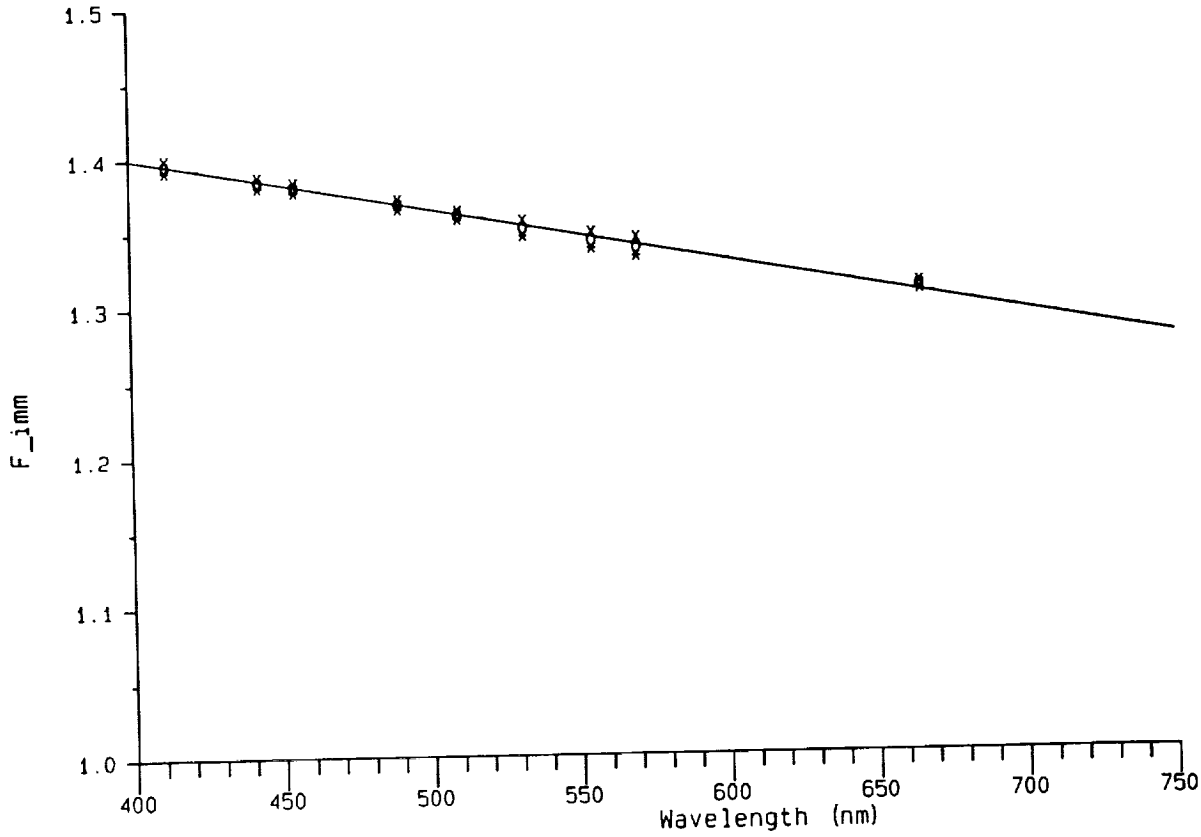

Fig. 8. Immersion coefficients from replicate immersion tests on the MER-2040 (S/N 8738) E_d channels. The legend in the figure provides experimental dates and lamp-to-collector distances. The solid line is the least-squares regression fit to the mean coefficients

Table 9. Linear regression fits to immersion coefficients, as expressed in (1), for irradiance collectors on several MER underwater radiometers manufactured by BSI. In addition, the squared correlation coefficient, R^2, and the residual standard deviation, s_{xy}, are listed.

MER		*Number of*	*Measurement*	*Regression Coefficient*			
Model	S/N	*Channels*	*Type*	a	b	R^2	s_{xy}
1012	8107	7	E_d	1.4745	2.6759	0.900	0.010
1032	8301	11	E_d	1.5833	4.0050	0.980	0.005
1032	8301	8	E_u	1.6496	5.1186	0.980	0.007
2040	8724	7	E_d	1.6084	4.3755	0.998	0.002
2040	8725	6	E_d	1.3826	1.0907	0.355	0.015
2040	8738†	12	E_d	1.5405	3.5163	0.998	0.002

† MER-2040 S/N 8738 is equipped with a Teflon diffuser. All other instruments tested have Plexiglas diffusers.

Table 10. Statistics of variability between immersion coefficients for different irradiance collectors at selected wavelengths.

Wavelength	*Number of*	*Immersion Coefficient*		
±2 nm	*Collectors*	μ	σ	*Range*
406	3	1.3791	0.0346	0.0668
410	7	1.3966	0.0520	0.1513
442	8	1.3920	0.0377	0.1244
489	8	1.3744	0.0387	0.1157
555	3	1.3562	0.0113	0.0212
664	3	1.3194	0.0191	0.0382
670	5	1.3424	0.0419	0.0998

explained by experimental uncertainty in the characterization procedure. The observed scatter far exceeds the allowable uncertainty implied by the radiometric calibration goals (that is, 1% uncertainty) of the SeaWiFS Calibration and Validation Program. It is essential, therefore, to experimentally characterize immersion factors for every profiling irradiance sensor to be used as part of SeaWiFS validation.

Chapter 2

The Effect of Oxygen Absorption on Band-7 Radiance

ROBERT S. FRASER
NASA Goddard Space Flight Center
Greenbelt, Maryland

ABSTRACT

Atmospheric oxygen absorbs about 13% of the available sunlight reflected from the Earth in band 7 of the SeaWiFS instrument, which has a bandwidth spanning 745–785 nm. If a correction is made for the average amount of absorption, then the measured radiance would vary by ±0.004 for a two standard deviation (2σ) variability in the amount of oxygen in a vertical column. For comparison, the instrumental noise is about one-half, or 0.002, of this variation. A correction based on the regional changes in absorption, as a function of season, would not significantly reduce the statistical variation in absorption, but a correction based on surface pressure would be accurate.

2.1 INTRODUCTION

Atmospheric oxygen absorbs approximately 13% of the radiant energy in SeaWiFS band 7, which has a width spanning 745–785 nm. Since the total amount of oxygen is proportional to the surface pressure, the amount of oxygen varies directly with the variation in surface pressure. The standard deviation (1σ) of the surface pressure over the entire ocean is only about 1%. It is expected, therefore, that oxygen will cause a variability, equivalent to 2σ, in the radiance in band 7, i.e., about 0.02×0.13 =0.0026. This variability is about 1.5 times the instrument radiance noise (Hooker et al. 1992). The detailed analysis presented here supports this conclusion.

2.2 THEORY

The radiance (L_t), measured at a satellite, can be expressed as

$$L_t = L_{\text{atm}} + L_{\text{sfc}}, \tag{2}$$

where L_{atm} is the radiance of light reflected from the atmosphere, and L_{sfc} is the radiance of light leaving an ocean surface and passing through the atmosphere. Although L_{atm} receives contributions from light scattered throughout the atmosphere, a slightly more conservative approach to estimating the effect of oxygen absorption is to assume that the scattering occurs in a thin layer near the surface, and that the absorbing oxygen lies entirely above the surface layer.

In this simulation, sunlight is considered to reflect from both the sea surface and a concentrated layer of air just above the sea surface. The combined reflectance (for the sea surface and the layer of air) is equal to ρ. Light would be absorbed along a two-way path through the entire atmosphere. Then the total radiance measured by the SeaWiFS instrument (in orbit) would be

$$L_t = \int \rho(\lambda) f(\lambda) T(\lambda) S(\lambda) d\lambda, \tag{3}$$

where f is the instrument spectral response function, S is the solar spectral irradiance, T is the two-way transmission through the volume of oxygen

$$T(\lambda, \theta, \theta_0) = e^{-m(\theta,\theta_0)\tau_{\text{ox}}(\lambda)} \tag{4}$$

where τ_{ox} is the oxygen absorption optical thickness, and m represents the air mass:

$$m = \frac{1}{\cos\theta_0} + \frac{1}{\cos\theta}. \tag{5}$$

In (5), θ_0 is the solar zenith angle, and θ is the zenith angle of the line-of-sight in a plane-parallel atmosphere. In (4), the oxygen absorption optical thickness, $\tau_{\text{ox}}(\lambda)$, is defined as

$$\tau_{\text{ox}}(\lambda) = k(\lambda) N, \tag{6}$$

where k is the molecular absorption cross-section area, and N is the total number of oxygen molecules per unit area in a vertical column of the atmosphere.

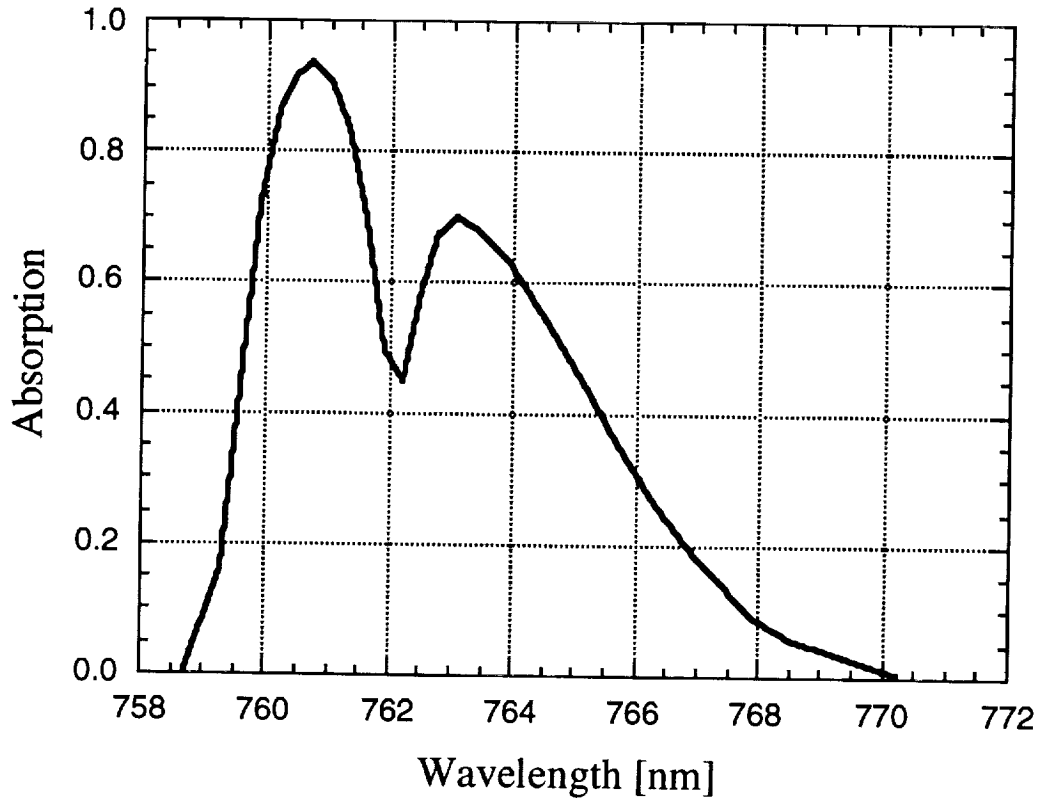

Fig. 9. Oxygen absorption band (A-band), the integrand of (13), for an air mass $m = 2$. The curve is adapted from data given by Wu (1985).

Two models, one with oxygen and another without oxygen, will be examined and compared with regard to the radiance SeaWiFS will measure in orbit. In the model without absorbing oxygen, L_0 represents the radiance. The number of absorbing molecules above the reflecting layer, N, is then equal to 0, the optical thickness τ=0, the transmission T=1, and from (3) the radiance is

$$\begin{aligned} L_0 &= \rho S(\lambda_1) \int f(\lambda) d\lambda \\ &= \rho S(\lambda_1) B. \end{aligned} \tag{7}$$

In this expression, the reflectance, ρ, can be considered constant without loss of generality, and $S(765)$ has a value of $122.5\,\mathrm{mW\,cm^{-2}\,\mu m^{-1}}$ when λ_1 is equal to 765 nm. The width of band 7, B, is approximately 40.5 nm, as defined by the integrated SeaWiFS spectral response function, $f(\lambda)$, supplied by Barnes (1994). The wavelength $\lambda_1 = 765$ nm is selected so that (3) and (7) are equal.

If oxygen absorption is accounted for, the radiance, L, of light transmitted through the absorbing oxygen along a two-way path is, from (3) and (4),

$$L = \int \rho(\lambda) f(\lambda) e^{-m(\theta,\theta_0)\tau(\lambda)} S(\lambda) d\lambda. \tag{8}$$

With $T = 1$ in (3), the absorbed radiation is then found as the difference between (3) and (8):

$$\Delta L = L_0 - L, \tag{9}$$

$$= \int \rho(\lambda) f(\lambda) \left[1 - e^{-m(\theta,\theta_0)\tau(\lambda)}\right] S(\lambda) d\lambda, \tag{10}$$

$$= \rho f(\lambda_2) S(\lambda_2) \int \left[1 - e^{-m(\theta,\theta_0)\tau(\lambda)}\right] d\lambda, \tag{11}$$

$$= \rho f(\lambda_2) S(\lambda_2) W, \tag{12}$$

$$W = \int \left[1 - e^{-m(\theta,\theta_0)\tau(\lambda)}\right] d\lambda, \tag{13}$$

with the following values in effect: $\lambda_2 = 764$ nm, $f(\lambda_2) = 0.94$, and $S(\lambda_2) = 124\,\mathrm{mW\,cm^{-2}\,\mu m^{-1}}$. Note that λ_2 is a wavelength within the absorbing band ($758 < \lambda_2 < 771$ nm) and not within the total band (735–800 nm). The integral in (13) represents an equivalent bandwidth, W, of complete absorption and depends on the amount of oxygen. The integrand of (13) is given in Fig. 9. The absorption band is restricted to a width of 13 nm ($758 < \lambda < 771$ nm).

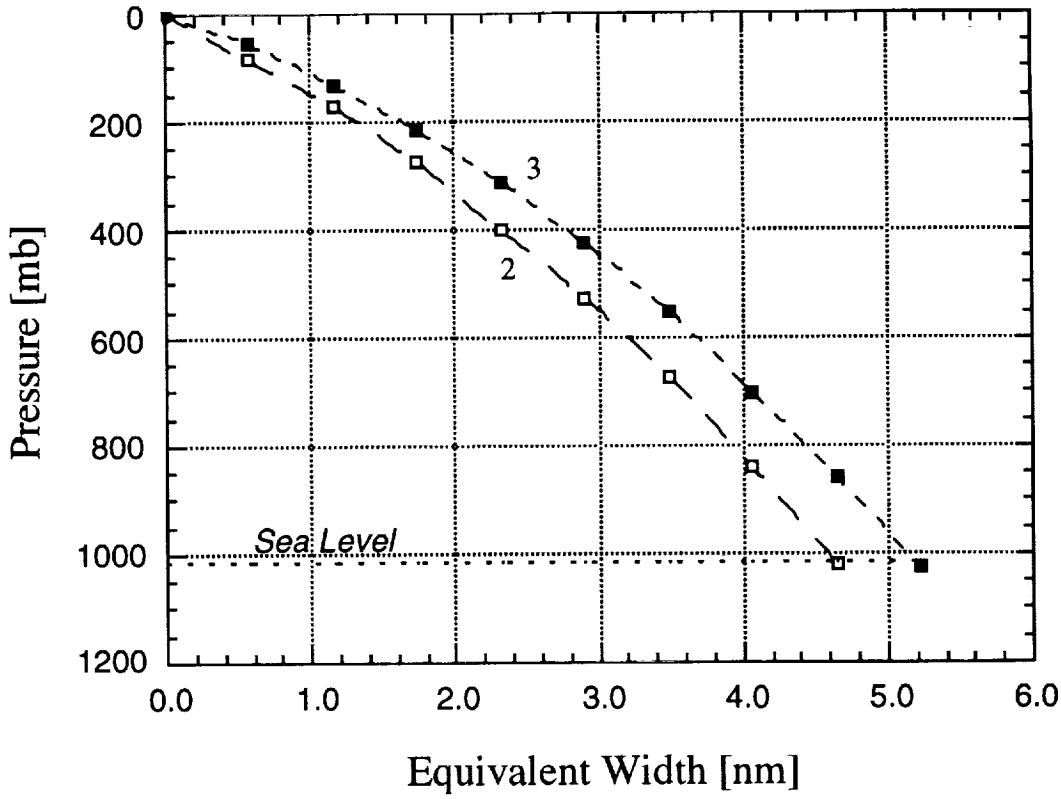

Fig. 10. The equivalent width, W, of the oxygen A-band for sunlight reflected from surfaces at increasing pressure levels in the atmosphere. Curves are given for air masses 2 and 3. This figure is adapted from computations made by Curran (pers. comm.).

Table 11. Equivalent width, W, of oxygen A-band for sunlight passing to the surface (1,013 mb) and reflected into space. The data presented are taken from Fig. 10. The symbol p represents surface pressure.

Air Mass	W [nm]	$\Delta W/\Delta p$ [nm/mb]	*Fractional Absorption* W/B
2	4.6	0.0031	0.11
3	5.2	0.0035	0.13

The change in W with respect to the total surface pressure of all atmospheric gases (N_2, O_2, etc.) is shown in Fig. 10. Table 11 gives W for band 7, calculated for sunlight reaching sea level and then reflected to space. The change in W with respect to pressure appears in the third column, and the fraction of energy absorbed in band 7, from (15), appears in the last column.

The relative loss of radiance caused by oxygen absorption is found by dividing (12) by (7):

$$\frac{\Delta L}{L_0} = \frac{\rho f(\lambda_2) S(\lambda_2) W}{\rho S(\lambda_1) B} = \beta \frac{W}{B}, \tag{14}$$

where for air mass $m = 2$,

$$\beta = \frac{f(\lambda_2) S(\lambda_2)}{S(\lambda_1)} = \frac{0.94 \times 124}{122.5} = 0.95. \tag{15}$$

The relative amount of absorbed energy taken out of the band is approximately that given by letting $\beta = 1$ in (14):

$$\frac{\Delta L}{L_0} = \frac{W}{B}. \tag{16}$$

The relative loss in radiance equals the ratio of the equivalent width W of the oxygen band, to band 7 width B.

The change in the equivalent bandwidth caused by a change in the amount of oxygen can be calculated from (14):

$$\frac{\Delta L}{L_0} = \frac{\Delta W}{B} = \frac{\Delta W}{\Delta p} \frac{\Delta p}{B}, \tag{17}$$

where p is the total sea level pressure of all atmospheric gases, i.e., surface pressure.

Statistical data on the atmospheric surface pressure are not available with high spatial and temporal resolution. The median value of pressure over the oceans is 1,012.5 mb, and the extreme monthly values are 969 and 1,043 mb (McClain et al. 1994). The extremes and reference pressure (p_{ref}) data are given in Table 12. The deviations of −44 and +30 mb are the changes of the monthly extreme pressures from 1,013 mb (United States Navy 1978). The maximum presssure variations occur in the middle latitudes during the winter. The deviations of −30 and +34 mb, appearing in the last column of the second row, are based on the maximum data given by Cantor and Cole (1985); the deviations are computed as the local average ($\pm 2\sigma$) minus the worldwide average. For example, the *All ocean deviations*=1,015 ± 32 − 1,013 = −30, +34 mb. The tropical deviation for a 2σ variability in pressure (−6, +2 mb) is much weaker. Because extreme low-pressure cyclones are associated with strong winds, rain, and overcast clouds, satellite observations of the surface would not be possible under such conditions.

Table 12. Sea level pressure data for oxygen absorption estimation. The deviation column values (p_{dev}) are the differences between the minimum and maximum surface pressures compared to 1,013 mb.

Statistical Basis	p_{ref} [mb]	p_{dev} [mb]
All-ocean average†	1,015	−30, +34
Monthly extreme low	969	−44
Monthly extreme high	1,043	+30
Tropics†	1,011	−6, +2

† Cantor and Cole (1985); all others from McClain et al. (1994).

Absorption changes caused by extreme variations in oxygen absorption are given in Table 13 for air masses 3 and 4. The minimum (−44 mb) and maximum (+34 mb) pressure changes are taken from Table 12. The changes in equivalent bandwidth ($\Delta W/\Delta p$) are taken from Table 11 for air mass 3 and extrapolated for air mass 4. The magnitude of the variations is 0.003–0.004, which can be compared with the instrumental noise, 0.002, estimated from the signal-to-noise ratio (SNR) for band 7 (Hooker et al. 1992). As seen from Table 12, the small pressure variations in the tropics would have a small effect on absorption changes in band 7.

Table 13. Absorption changes for band 7.

Air Mass	$\Delta W/\Delta$p [nm/mb]	p_{dev} [mb]	W	*Absorption Change*
3	0.0035	−44	−0.15	−0.004
3	0.0035	+34	+0.12	+0.003
4	0.0041	−44	−0.18	−0.004
4	0.0041	+34	+0.14	−0.003

2.3 CONCLUSION

The simplest correction for oxygen absorption is based on a constant amount of atmospheric oxygen in a vertical direction. In this case, oxygen absorbs about 13% of the radiant energy available for remote sensing by SeaWiFS band 7. The absorption depends on the length of the path through the atmosphere: from the sun [i.e., total solar irradiance at the top of the atmosphere (TOA)] to the surface, and back to SeaWiFS. Even if the amount of oxygen in a vertical direction is assumed to be constant, oxygen corrections have to be adjusted for the geometry. Statistical data are not available for making a precise estimate of the variation in absorption caused by the change in the amount of oxygen that occurs when the atmospheric pressure varies from an average value of 1,013 mb. For a 2σ variation in the amount of oxygen, however, the variable absorption in band 7 is not more than twice the instrumental noise.

The operational procedure for making an atmospheric correction for molecular scattering will use the surface pressure in the correction algorithm. This pressure data can also be utilized to make a correction for oxygen absorption. In this case, the statistical variations discussed here would not occur.

In the above discussions, the vertical gradient of atmospheric optical properties has been neglected, but Ding and Gordon (1994) have shown that the vertical profile must be included for the derivation of the water-leaving radiance to be sufficiently accurate. Corrections based on a single reference profile are adequate except for the following three cases: large amounts of stratospheric aerosol, such as occurred after the volcanic eruptions of El Chichón and Mount Pinatubo; thin cirrus clouds; and aeolian dust, such as that from the Sahara or Gobi Deserts.

Chapter 3

Second SeaWiFS Preflight Solar Radiation-Based Calibration Experiment

STUART F. BIGGAR
KURTIS J. THOME
PHILIP N. SLATER
Remote Sensing Group, Optical Sciences Center
University of Arizona, Tucson, Arizona

ALAN W. HOLMES
Santa Barbara Research Center
Goleta, California

ROBERT A. BARNES
ManTech, Inc.
Wallops Island, Virginia

ABSTRACT

This paper describes the second solar radiation-based calibration of SeaWiFS. The experiment was done on 1 November 1993 in the rock garden at SBRC. The results of the calibration are presented, along with a comparison to the SIS calibration done at SBRC. The estimated uncertainty of the SIS calibration is 2.8%, compared to the 4% estimated uncertainty for the solar-based calibration. There is also an uncertainty in the value of the exoatmospheric solar irradiance used to make this comparison, which is probably on the order of 1%. In addition, the integrated out-of-band blocking for SeaWiFS is in the 1–3% range, which can introduce significant differences between the lamp- and solar-based calibrations. This agreement is better than anticipated, and better than the agreement achieved in March 1993 from the first experiment. The better agreement is probably due to a sphere recalibration between the two experiments.

3.1 INTRODUCTION

The basic concept for a solar radiation-based calibration of a satellite sensor is to attempt to simulate the solar irradiance incident on the diffuser in space while doing the experiment on the ground. A thorough discussion of the concept was presented in April 1993 at the Society of Photo-optical Instrumentation Engineers (SPIE) meeting in Orlando, Florida (Biggar et al. 1993). This presentation included results from the first calibration performed on SeaWiFS. After this calibration, a stray light, or transient response, problem was discovered in SeaWiFS. The sensor was subsequently modified to reduce the response to out-of-field radiation, such as that caused by clouds, within 10 pixels of the SeaWiFS instantaneous field-of-view (IFOV). After the modifications, the sensor was recalibrated in the laboratory using the 100 cm SIS at SBRC. Another solar radiation-based calibration was scheduled for late October 1993, to coincide with a look at the full moon on 29 October. Cloud and visibility conditions, caused in part from haze and smoke from fires in the Southern California area, prevented the calibration from taking place on 29–31 October. On 1 November, sky conditions were good enough for calibration purposes. The sensor was taken outside at about 1115 Pacific Standard Time (PST), and measurements were taken at about 1215, 1255, and 1400 PST. The instrument was covered immediately after the last data set was collected.

3.2 EXPERIMENTAL METHOD

The transmittance along the path to the sun was measured with a solar radiometer possessing 10 bands covering the spectral range of about 370–1,040 nm. Table 14 shows representative radiometer data for the nine bands that were not affected by water vapor absorption. The sky conditions on 1 November 1993 were not sufficiently favorable to allow a Langley plot determination of the optical depth; therefore, *instantaneous* measurements of the transmittance were made by using previous calibrations

Table 14. Solar radiometer optical depth measurements.

Band Number	*Wavelength* [nm]	*Optical Depth*	σ
1	368.9	1.0109	0.0061
2	399.1	0.8279	0.0070
3	440.0	0.6623	0.0061
4	518.6	0.4633	0.0050
5	608.5	0.3499	0.0045
6	669.0	0.2756	0.0039
7	779.7	0.2008	0.0033
8	869.8	0.1643	0.0028
10	1,027.2	0.1284	0.0020

Table 15. SeaWiFS measurements on 1 November 1993 at 1400 PST. Pixel 312 (the center pixel) and pixel 0 (zero offset) were used for the determinations of the total and *diffuse only* signals.

Band Number	*Shaded* (zero offset)	*Shaded* (312)	*Unshaded* (zero offset)	*Unshaded* (312)	*Diffuse/ Global*	Δ *Unshaded vs. Shaded*
1	20	60	20	254	0.17094	194
2	17	58	17	294	0.14801	236
3	20	52	20	282	0.12261	229
4	20	55	20	332	0.11218	277
5	22	60	22	421	0.09520	361
6	24	60	24	508	0.07438	448
7	24	55	24	508	0.06405	453
8	21	58	21	591	0.06491	533

of the instrument zero-airmass intercept. Measurements by the same solar radiometer were also made, after the calibration described here, during subsequent satellite calibration campaigns at White Sands National Monument in New Mexico. For the intercepts done before and after the solar radiation-based calibration, the standard deviation (σ) is about 1% of the intercept value. It is expected that the error in the transmittance measurement when using these intercepts will be less than approximately 3% at the measurement wavelengths.

The optical depths and the barometric pressure are used to separate the optical depth components due to Rayleigh scattering, aerosol scattering and absorption, and absorption due to ozone (Biggar et al. 1990). The procedure employed here assumes a Junge power law distribution for aerosol particle size. The results on 1 November give a Junge parameter of 3.50–3.43, and a derived columnar ozone amount of 0.246–0.260 cm-atm† for the three measurement times. Using the Junge parameter, ozone amount, and the barometric pressure, the optical depth components can be computed for each of the SeaWiFS bands. MODTRAN was used to compute the effects of gaseous absorption for each band. The only band that exhibits any significant absorption is band 7, and the oxygen slant path transmittance for this band is computed to be 0.927.

The transmittance measurements described above were performed when the sensor was actually taking data from the illuminated solar diffuser. Measurements of the diffuser were made with the diffuser illuminated by the sun and the sky (unshaded), and by only the sky (direct beam blocked, or shaded). Data from pixel 312, the center pixel from the diffuser, along with that from pixel 0 (the zero offset) were used to determine the total and *diffuse only* signals. The choice of pixel 312 is not critical, as the variation across the diffuser is no more than one digital count (DC) for any band.

3.3 RESULTS

The measurements from the diffuser are presented in Table 15. These data are from the 1400 PST measurement sequence. The data in the table include the zero offset for each band for both the shaded and unshaded measurements, the actual measurements, and two computed

† The *centimeter-atmosphere* (cm-atm) is a measure of trace gas columnar amount. It can be envisioned as if the entire trace gas content within a $1\,cm^2$ column of the Earth's atmosphere was accumulated at the base of this column under standard temperature and pressure conditions. The cm-atm would give the length of this volume of gas in centimeters.

Table 16. Transmittance and predicted DCs in orbit.

Band Number	*Vertical Path*	*Slant Path*	*Predicted TOA DCs*
1	0.4651	0.2860	677.5
2	0.5274	0.3512	671.1
3	0.6004	0.4342	526.8
4	0.6238	0.4622	598.7
5	0.6654	0.5136	702.2
6	0.7575	0.6349	705.1
7	0.7507	0.6565	689.7
8	0.8437	0.7573	703.5

Table 17. Sphere calibration computations.

Band Number	*Integrated Irradiance (E)*	*Calibration*	*BRDF†*	*Spectral Correction*	*Offset*	*Predicted DCs*
1	170.827	0.00704	0.02682	0.963	20	695.8
2	188.992	0.00810	0.02786	0.983	17	678.3
3	193.383	0.01045	0.02751	0.980	20	539.5
4	189.022	0.00923	0.02806	0.998	20	595.8
5	187.431	0.00744	0.02755	0.991	22	722.4
6	151.546	0.00629	0.02800	1.011	24	691.3
7	121.715	0.00512	0.02854	0.995	24	705.9
8	98.168	0.00422	0.03011	1.011	20	712.8

† Bidirectional Reflectance Distribution Function

quantities—the ratio of the diffuse signal to the global (or total) signal, and the difference between unshaded and shaded measurements. This difference is the direct solar beam signal without the diffuse sky contribution.

A forward-scatter correction must be made to account for the small amount of forward-scattered diffuse light that is blocked by the disk. This corrected measurement of the direct solar beam is then further corrected for the transmittance in order to compute an expected solar diffuser measurement at TOA, i.e., in orbit. The forward-scatter correction is wavelength dependent, but in all cases it is very small, i.e., less than 1 DC. This correction is subtracted from the difference in measurements.

The DCs for each SeaWiFS band are then divided by the slant path transmittance, which has been computed for each band. This transmittance is computed with Beer's Law, using the optical depth components in each band, and further multiplied by the oxygen transmittance in band 7. The transmittance values computed for each band are given in Table 16. These values correspond to a time of 14:00:30 and an effective airmass of 1.6354. The uncertainty in airmass for a five-minute period around this time is 0.0079, which corresponds to an uncertainty in transmittance of less than 0.5%.

The predicted DCs have some associated uncertainties, which can be difficult to quantify. The major source of uncertainty is the transmittance measurement. Other sources of uncertainty are interpolation from the radiometer wavelengths to the SeaWiFS wavelengths, the forward-scatter correction, the oxygen transmittance computation for band 7, and atmospheric variability. The transmittance measurement uncertainty is probably less than 3%, as this uncertainty is dependent on the radiometer calibration. The interpolation uncertainty can be estimated by using the calculated optical-depth components to compute the expected transmittance, which was also measured in the solar radiometer bands. The largest difference is for band 4 of the radiometer, and it corresponds to an error in transmittance of about 0.9%. The second error term in Equation 3 of Biggar et al. (1993), representing the airmass uncertainty, is less than 0.2% for all bands. The atmospheric variability can be estimated by comparing the standard deviation of the transmittance measurements to the average. The variability in transmittance in the radiometer bands was about 1%. The average transmittance was used so that this variability should not cause a significant uncertainty. A total uncertainty on the order of 4% is expected, with the radiometer calibration being the dominant term. The solar radiometer gives a much more repeatable measurement, so it would be better if the sky conditions were stable enough for a Langley plot determination of the transmittance. Conditions in Santa Barbara were not good enough, however, for such a determination.

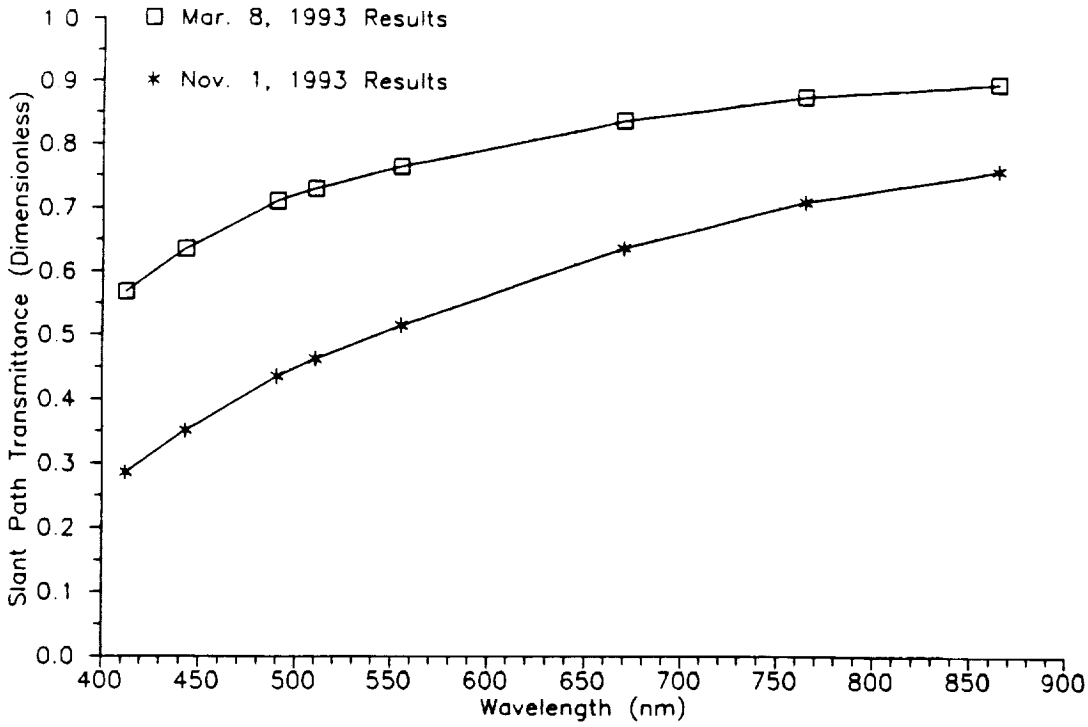

Fig. 11. Measured atmospheric transmittances during the two solar calibration experiments. The transmittances are given at the wavelengths of the Arizona solar radiometer.

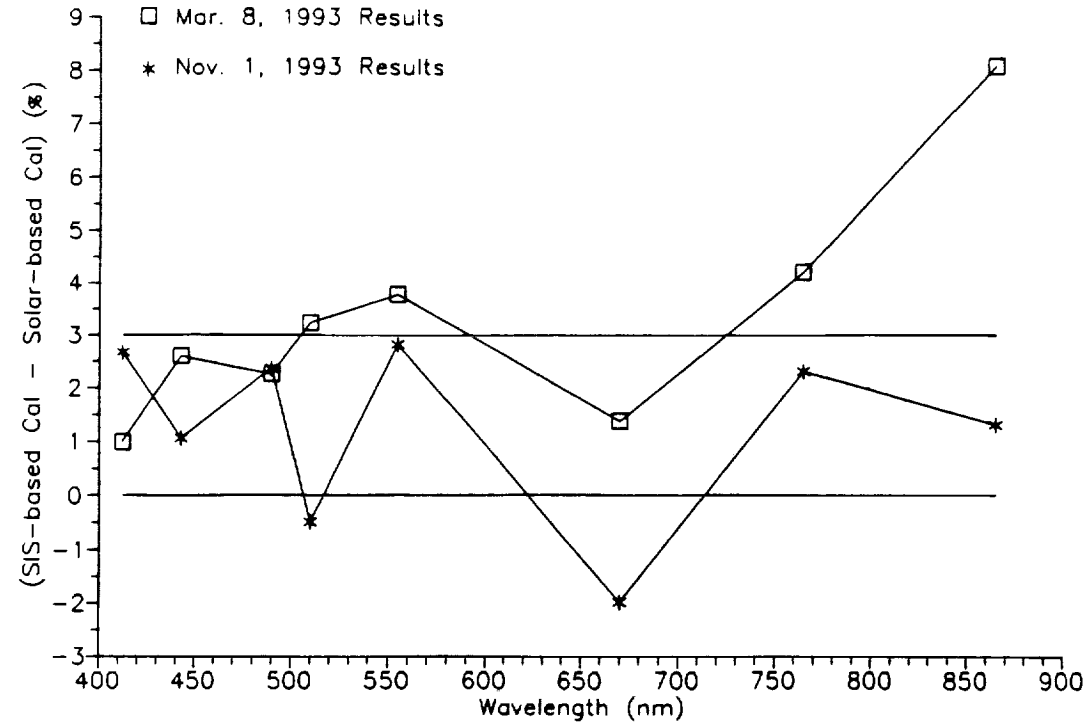

Fig. 12. Comparison of the laboratory- and solar-based calibrations of SeaWiFS. The laboratory measurements were made by SBRC with a 100 cm SIS. For the 1 November 1993 solar calibration, the two techniques agreed to better than 3%.

3.4 DISCUSSION

As a check on the results, and in an effort to relate these results to the International System of Units (SI†), these results were compared to the calibration of the SeaWiFS system with the SBRC 100 cm SIS. The SIS results were taken from the SeaWiFS Calibration and Acceptance Data Package, which is described in Barnes et al. (1994). Exoatmospheric solar irradiance data, based on Neckel and Labs (1984), were used; these data were integrated over the SeaWiFS band and then divided by the radiance-to-DC calibration. This value was then multiplied by the diffuser BRDF and divided by the correction for spectral shape. The zero signal offset was then added to give the predicted TOA DC value. The results are summarized in Table 17. The results in Table 17 can be easily compared to those in Table 16. The summary of this comparison is shown in Table 18.

For all bands, the differences between the solar-based and sphere-based methods are less than 3%. The estimated uncertainty of the SIS calibration is 2.8%, compared to the 4% estimated uncertainty for the solar-based calibration. There is also an uncertainty in the value of the exoatmospheric solar irradiance used to make this comparison, which is probably on the order of 1%. In addition, the integrated out-of-band blocking for SeaWiFS is in the 1–3% range, which can introduce significant differences between the lamp- and solar-based calibrations.

This agreement is better than anticipated, and better than the agreement achieved in March 1993 for the first experiment. The better agreement is probably due to a sphere recalibration between the two experiments.

It is also instructive to compare the SeaWiFS band transmittances from the two dates (Fig. 11). The atmosphere was clearer in March compared to late October, when smoke from fires in the Los Angeles area affected conditions in Santa Barbara. The measurements in March were also at a lower solar zenith angle than in November. Both of these factors could possibly make the November data more uncertain; however, the results still compare well with laboratory measurements. This favorable comparison leads to the conclusion that the transmittance measurements are fairly accurate even though a Langley plot was not possible. Figure 12 shows the percentage difference between the calibration methods for the two dates.

Table 18. Comparison between solar radiation-based and laboratory (SIS based) calibrations.

Band Number	*Solar Based*	*SIS Based*	*Difference* [%]
1	677.5	695.8	2.6
2	671.1	678.3	1.1
3	526.8	539.5	2.3
4	598.7	595.8	−0.5
5	702.2	722.4	2.8
6	705.1	691.3	−2.0
7	689.7	705.9	2.3
8	703.5	712.8	1.3

† The SI acronym is derived from the original French title, *Systéme International d' Unités.*

Chapter 4

In Situ Evaluation of a Ship's Shadow

CHRISTIAN T. WEIR
DAVID A. SIEGEL
DAVID W. MENZIES
University of California at Santa Barbara
Santa Barbara, California

ANTHONY F. MICHAELS
Bermuda Biological Station for Research
Ferry Reach, St. George's, Bermuda

ABSTRACT

In situ measurements of optical properties made from a ship can be biased by the ship's shadow. In an effort to evaluate the ship shadow perturbation created by the R/V *Weatherbird II,* profiles of downwelling irradiance, $E_d(z,\lambda)$; upwelling radiance, $L_u(z,\lambda)$; as well as derived AOPs were obtained at four distances—1 m, 3 m, 6 m, and 20 m or more—off the ship's stern. Two statistical analyses of these data are explored here. The first analysis uses data from pairs of simultaneously-obtained light profiles, one profile obtained at a distance greater than 20 m from the stern of the ship, and the other taken either 1 or 6 m off the stern. The second analysis compares the derived AOPs for each profiling distance from the ship, using data obtained throughout the length of the experiment. Significant differences are rare in comparisons of profiles obtained at least 3 m off the ship's stern. At 1 m off the stern, however, significant discrepancies are intermittently observed. This work illustrates that the inherent sources of noise in determining radiative fluxes and AOPs in the upper ocean are generally greater than the effects incurred by the ship's own shadow under optimal conditions.

4.1 INTRODUCTION

Accurate measurements of AOPs are required to develop a detailed understanding of the processes regulating bio-optical property distributions and their relationship to remotely sensed signals. Instrumentation designed to measure properties of the underwater radiation field, when deployed at relatively close proximity to a ship, may encounter perturbations caused by the ship's shadow (e.g., Poole 1936, Strickland 1958, Gordon 1985, Voss et al. 1986, Waters et al. 1990, and Helliwell et al. 1990). This source of error is of obvious importance and must be accurately assessed. Poole (1936) estimated that the ship shadow error under diffuse skylight is about 10% at a depth of 5 m when the radiometer is deployed approximately 2 m off the stern, and also noted that this source of error decreases in significance with increasing depth. The Monte Carlo simulations performed by Gordon (1985) indicate that the error in downwelling irradiance rarely exceeds 2% as long as skies are clear and the sun is within 45° of the stern. At low solar elevations, however, these errors can increase to about 10%. Gordon (1985) also shows that the errors are reduced as the instrument is moved horizontally away from the ship, although errors during diffuse light conditions may remain as high as 30%. Voss et al. (1986) conducted an experiment with an extendable sea-going crane that showed values of upwelling radiance, $L_u(z,\lambda)$, decrease by 10–20% unless the instrument is deployed more than 5 m from the ship.

Ship shadow perturbations are likely to be the greatest near the sea surface. This factor is critical for the development of ocean color algorithms, as maximum accuracy must be sought for the determination of *calculated* parameters such as the remote sensing reflectance, $R_{rs}(\lambda)$. Several studies have attempted to completely avoid the ship's shadow by floating optical instrumentation a considerable distance from a ship (Gordon and Clark 1980, Clark 1981, and Waters et al. 1990). These deployment strategies are difficult to conduct operationally, particularly in rough seas. Such strategies also place severe limits on the

Editors' Note: This chapter originally appeared as an article in *Ocean Optics XII,* published by SPIE (Weir et al. 1994), and is being included in this volume with the permission of the authors and SPIE. Minor editorial changes have been made to reflect the style of *The SeaWiFS Technical Report Series.*

amount of data that can be collected, restrict linkages to other oceanographic observations, and limit time-scale resolution, e.g., Dickey and Siegel (1993).

In order to completely avoid the ship's shadow when measurements of downwelling irradiance, $E_d(z,\lambda)$, are being made, Mueller and Austin (1992 and 1995) suggest that the deployment of optical instrumentation should be at a distance, ξ_d. Mueller and Austin (1992 and 1995) define ξ_d using

$$\xi_d = \frac{\sin(48.4°)}{K_d(\lambda)}, \tag{18}$$

where $K_d(\lambda)$ represents the vertical attenuation coefficient for downwelling irradiance. Typical values for $K_d(\lambda)$ off Bermuda range from 0.02–0.08 m^{-1} (Siegel et al. 1994), which result in recommended deployment distances of 9–40 m from a ship's stern. Similarly, recommendations for deployment distances for $E_u(z,\lambda)$ and $L_u(z,\lambda)$ (ξ_u and ξ_L, respectively) are given by Mueller and Austin (1992 and 1995) as

$$\xi_u = \frac{3}{K_u(\lambda)}, \tag{19}$$

and

$$\xi_L = \frac{1.5}{K_L(\lambda)}, \tag{20}$$

where $K_u(\lambda)$ and $K_L(\lambda)$ are the vertical attenuation coefficients for upwelled irradiance and radiance, respectively. Values of $K_u(\lambda)$ and $K_L(\lambda)$ are roughly equal to values of $K_d(\lambda)$. Typical values of ξ_u and ξ_L are usually greater than 30 m, which is nearly the length of the ship used in this study. The distances recommended by (18)–(20) are based only on geometric relations, and are independent of ship size, sky conditions, sea state, deployment method, and the orientation of the ship with respect to the solar beam.

In this study, the effects of ship shadows upon data collected from the R/V *Weatherbird II*—length 35.05 m, beam 8.53 m, and draft 2.60 m—are examined. The *Weatherbird II* is used by the Bermuda Bio-Optics Project (BBOP) to make routine spectroradiometer casts in conjunction with the Joint Global Ocean Flux Study (JGOFS) Bermuda Atlantic Time-Series Study (BATS). Spectroradiometer profiles were made using an extendable boom to deploy the BBOP package, which allowed profiles to be made up to 6 m off the stern of the *Weatherbird II*. These data are compared with data collected using the optical free-falling instrument (OFFI) described by Waters et al. (1990). The OFFI data provide a *control* which can be used to search statistically for the effects of the ship's shadow. The measurements used were made under optimal conditions (i.e., clear skies, stern-to-ship solar orientation, near-constant illumination, etc.), and thus, provide the basis for evaluating the role of the ship shadows in developing ocean color remote sensing algorithms using the BBOP data set.

4.2 EXPERIMENTAL METHODS

The observations presented here were made from the *Weatherbird II* off Bermuda on 7 July and 9–10 July 1992. Two underwater spectroradiometers—the BBOP and the OFFI—were lowered simultaneously from the *Weatherbird II* to about 50 m (Fig. 13). The BBOP package consisted of a BSI MER-2040 underwater spectroradiometer, interfaced with a SeaTech transmissometer, chlorophyll fluorometer, and SeaBird conductivity, temperature, and pressure sensors (Siegel et al. 1994). The OFFI is a modified BSI MER-2020 underwater unit with a case outfitted with buoyant fins to provide stability and control in its descent rate (Waters et al. 1990).

The BBOP was lowered at three distances off the stern (1, 3, and 6 m) using the extendable boom. The OFFI was fished out, i.e., deployed astern of the ship, at least 20 m before descent. Profiles were made simultaneously so that instantaneous fluxes from the two instruments could be compared. Both instruments were deployed with the sun off the stern so that the ship's shadow trailed away and behind, which is part of the normal BBOP sampling procedure. Both instruments sampled $E_d(z,\lambda)$ and $L_u(z,\lambda)$ in spectral wavebands centered at 410, 441, 488, 520, and 565 nm.

Using laboratory facilities at the University of California at Santa Barbara (UCSB), radiometric calibrations were performed on both instruments two weeks prior to, and two months after, this cruise. The same calibration lamp (UCSB lamp F-303) was used for both calibrations. The calibration coefficients for the BBOP instrument varied by less than 0.5% for irradiance, and less than 3% for radiance, between both calibration dates. The OFFI calibration coefficients differed by 1–4% for both the irradiance and radiance channels. Calibration coefficients, which were obtained from the precruise determinations, were used for the analysis presented here.

The two individual bio-optical data sets were processed using the BBOP data processing system (Sorensen et al. 1994). The BBOP data processing system is used to:

1) Eliminate radiation values that are below a specified threshold;
2) Identify time segments where cloud perturbations are minimal;
3) Smooth specified channels of data and remove spikes, although not for $E_d(z,\lambda)$ or $L_u(z,\lambda)$; and
4) Bin the data into 1 m vertical depth bins.

The derived AOPs, such as $K_d(z,\lambda)$ and the remote sensing reflectance $R_{rs}(z,\lambda)$, are also calculated. In addition, the downwelling irradiance and upwelling radiance spectra just beneath the sea surface, $E_d(0^-,\lambda)$ and $L_u(0^-,\lambda)$, are determined by fitting profile data from the upper 20 m to the Beer-Lambert relation. Sorensen et al. (1994) gives a complete description of the BBOP data processing system and data handling procedures used by BBOP.

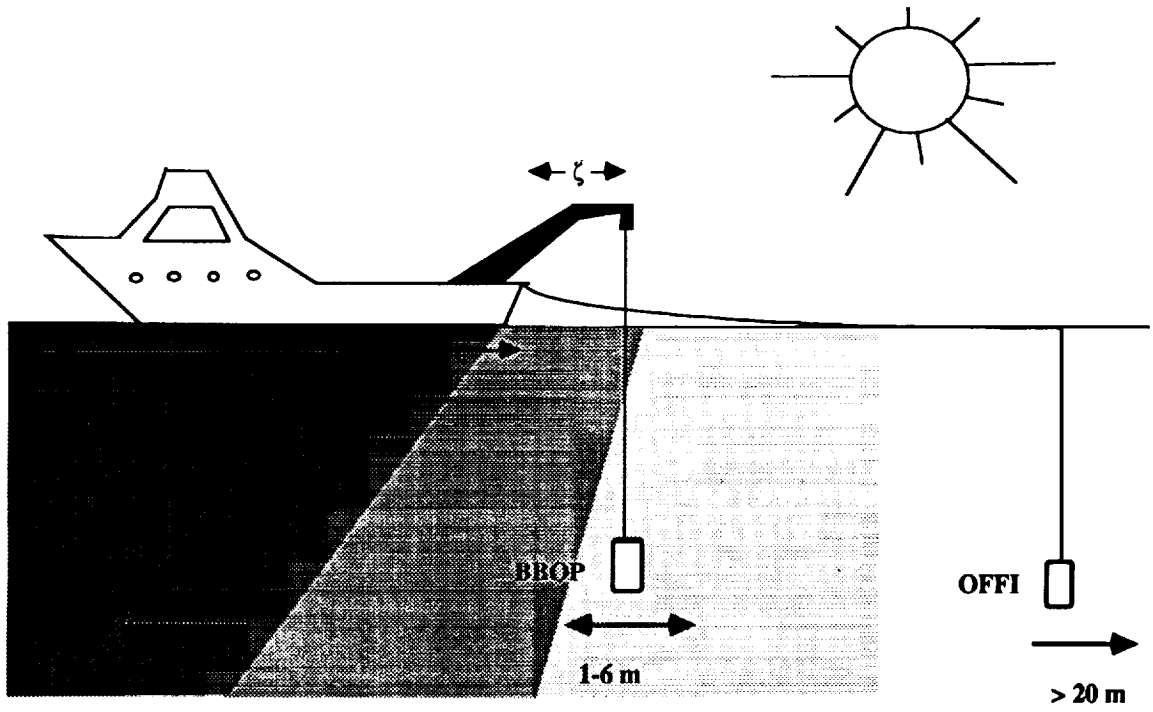

Fig. 13. Diagram of the BBOP ship shadow evaluation experimental design.

4.3 RESULTS

Two distinct statistical analyses are performed to evaluate the effects of the shadow cast by the R/V *Weatherbird II*. The first analysis compares the statistical differences between simultaneously sampled BBOP and OFFI data as the BBOP radiometer is deployed at various distances off the ship's stern. Differences between the two data sets are interpreted here to indicate the effects of the ship shadow, after accounting for a constant calibration error and the occurrence of random errors, i.e., noise. This analysis will be referred to as the *simultaneous* comparison. The second analysis, referred to as the *multi-distance* comparison, uses data obtained throughout the experiment to compare mean derived AOP values at each of the four distances (1, 3, 6, and greater than 20 m). The object of this comparison is to address whether any significant differences can be found among the AOP determinations.

4.3.1 Simultaneous Comparison

The simultaneous comparison evaluates the statistical difference between the fluxes and AOPs measured by the BBOP profiler at two distances off the ship's stern, and identical parameters determined using the OFFI profiler. The BBOP casts with $\xi = 1$ m are referred to as the B_1 casts, and the BBOP casts with $\xi = 6$ m are denoted as B_6. A total of 15 paired OFFI-BBOP casts, 7 B_6 and 8 B_1 casts, are used in this analysis. In the following discussion, the OFFI casts are designated O_{20}. Data from the two instruments are estimated to be collected *simultaneously* to within 5 sec. The statistical differences between OFFI (O_{20}) and BBOP (B_1 or B_6) measurements of downwelling irradiance, upwelling radiance, and derived AOPs are compared. A positive difference means that the BBOP measurements underestimate the O_{20} values, which may indicate a ship shadow influence. The error bars shown correspond to 90% confidence intervals (c.i.) for the mean estimates throughout the analysis.

For the experimental measurement of downwelling irradiance at 441 nm, there are no statistically significant differences (at the 90% confidence level) between the O_{20} casts and either the B_1 or the B_6 casts (Fig. 14, top). However, the B_1 mean differences are consistently positive, suggesting that the B_1 casts may be affected by the ship's shadow, although not in a statistically significant manner. The $B_1 - O_{20}$ difference increases as the sea surface is approached, which also suggests the signature of a ship shadow. The vertical profile of the $B_6 - O_{20}$ differences does not give any indication of a ship shadow influence. The other matching wavelengths (410, 488, 520, and 565 nm) for $E_d(z, \lambda)$ gave similar results, which are not shown here. The differences between the B_1 and O_{20} upwelled radiance data at 441 nm, $L_u(z, 441)$, are significantly different from zero and show a *ship shadow pattern* with depth, as the mean difference increases significantly towards the sea surface (Fig. 14, bottom). This divergence of the measurements is particularly apparent over the top 20 m, and the differences become smaller with increasing

depth. The $B_6 - O_{20}$ mean difference for $L_u(z, 441)$ shows no statistically significant pattern with depth. This observed reduction in ship shadow effects with distance from the ship is consistent with previous studies.

In terms of the derived AOPs $K_d(z, \lambda)$ and $R_{rs}(z, \lambda)$, no significant differences are found between either the B_1 or B_6 BBOP casts and the O_{20} data (Fig. 15). In particular, there are no consistent variations in these differences with depth that may be simply attributed to a ship shadow. This is true even for the mean $R_{rs}(z, \lambda)$ differences (Fig. 15, bottom) where the $O_{20} - B_1$ $L_u(z, \lambda)$ observations showed some deviations attributed to ship shadow. This lack of a signature in $R_{rs}(z, \lambda)$ may be due to the fact that both the $O_{20} - B_1$ $L_u(z, \lambda)$ and $E_d(z, \lambda)$ determinations are affected by the ship shadow. The decrease in both $L_u(z, \lambda)$ and $E_d(z, \lambda)$ due to the ship shadow, may actually cancel the effects of the shadow on values of $R_{rs}(z, \lambda)$.

Accurate measurement of both the upwelling and downwelling light streams just beneath the sea surface is critical to the development of algorithms for estimating bio-optical properties from satellite sensors. The differences between the O_{20} and B_1 or B_6 estimates of $E_d(0^-, \lambda)$ and $L_u(0^-, \lambda)$, for both the B_1 and B_6 distances off the stern, are shown in Fig. 16. The mean $E_d(0^-, \lambda)$ differences show no significant differences from zero, or between the two deployment distances (Fig. 16, top). Significant divergence from zero is found, however, for the mean $L_u(0^-, \lambda)$ differences for all wavelengths except 565 nm.

Significant differences are also found for some of the wavelengths in the $B_6 - O_{20}$ comparison, although it is unclear how large of a calibration difference remains between the two instruments. In particular, the size of the disparity in the mean differences between the two BBOP deployment distances increases as λ is decreased. These spectral observations are consistent with numerical results that indicate that the ship shadow effects scale as $c(\lambda)\,\xi$, where $c(\lambda)$ is the beam attenuation coefficient and ξ is the distance from the ship (Gordon 1985). The value of $c(\lambda)$ at 565 nm is likely to be larger than its value at 441 nm. These results further show that the influence of the ship's shadow will be more critical for the upwelling light stream rather than for downwelling light, as is expected. These results can be compared to Mueller and Austin (1992 and 1995).

4.3.2 Multi-Distance Comparison

The second analysis compares the mean values of derived AOPs using data obtained for each of the four distances (1, 3, 6, and greater than 20 m) throughout the experiment. All available casts are used for this analysis and the AOP determinations are classified by their distance from the stern of the *Weatherbird II*. The variations in K_d and R_{rs} at 441 nm with depth and deployment distance are shown in Fig. 17. Only rarely are there statistically significant differences (i.e., non-overlapping error bars), for the four deployment distances, though trends with distance are apparent. Similar results, not shown here, are found with the other wavelengths sampled by the BBOP.

Spectral differences in the remote sensing reflectance just beneath the sea surface, $R_{rs}(0^-, \lambda)$, can be used to surmise the spectral structure of the ship's shadow (Fig. 18). Again, no significant differences are found for any of the wavelengths. This analysis again suggests that the effects of the ship shadow on the upwelled light field may be effectively canceled out when normalized by the downwelling irradiance.

4.4 DISCUSSION

In order to correctly interpret the present results, it must be recognized that the observed mean differences are a composite of one or more signals: the actual ship shadow perturbation, a constant calibration difference between the OFFI and BBOP, and random errors due to the poor sampling of short time-scale noise (i.e., wave glint, small clouds, ship roll, and other effects). The influence of random noise can be reduced by averaging over many individual casts; however, the sample size for the simultaneous comparison is relatively small ($N = 7$ or 8). Comparisons between the pre- and post-cruise calibrations indicate the occurrence of only small calibration differences. The mean difference observed is, therefore, primarily composed of the ship shadow perturbation as modulated by an incompletely sampled random noise field. Elucidation of the ship shadow perturbation above this random noise element is the present goal.

The results of the simultaneous comparison show that there are no significant differences between the comparison of O_{20} $E_d(z, \lambda)$ values and either B_6 or B_1 irradiance determinations (Fig. 14, top). This result is consistent with the irradiance direct beam *cone* remaining off the stern (Gordon 1985 and Voss et al. 1986). The determination of upwelled radiance, however, clearly shows the effects of the ship shadow for the B_1 comparison, but not for the B_6 comparison (Fig. 14, bottom). A significant difference is also observed between the B_1 and B_6 mean $L_u(0^-, \lambda)$ differences (Fig. 16, bottom). At all wavelengths, B_1 mean differences were consistently larger than those calculated from B_6 data, with the O_{20} value being predictably and significantly greater than its simultaneous BBOP measurement. These results clearly show that BBOP data must be taken more than 1 m off the stern of the *Weatherbird II*, but does not have to be taken beyond 6 m, in order to avoid the ship's shadow perturbation.

The results of the multidistance comparison provide additional information for fine tuning of the distance criteria for the *Weatherbird II*. The derived AOP profiles showed little variability among the four different deployment distances. The multidistance comparisons support the notion that the effects of the ship's shadow may be effectively masked by random errors associated with the many sources

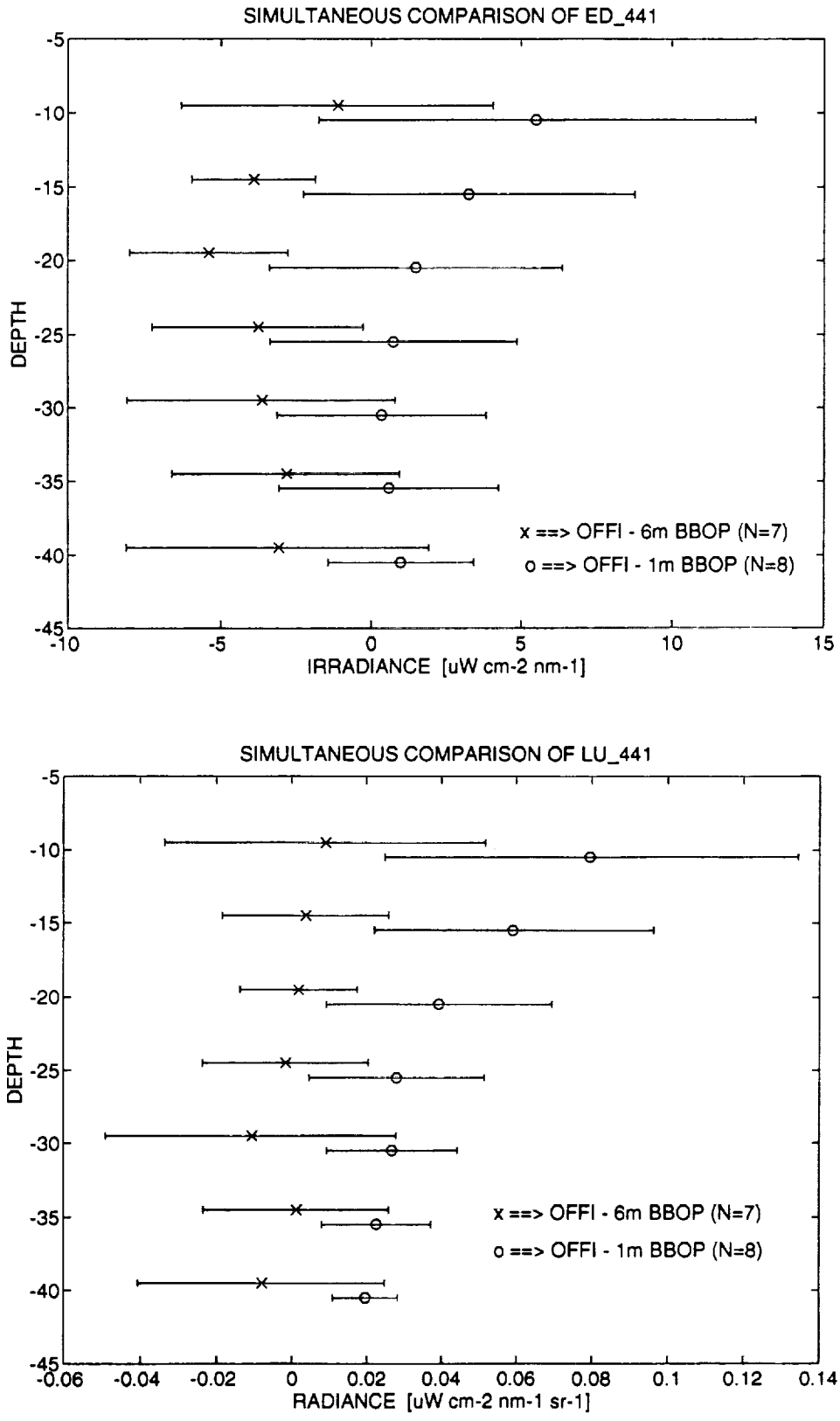

Fig. 14. Mean differences (with 90% c.i.) of simultaneous determinations of downwelling irradiance at 441 nm, shown in the top panel, and upwelling radiance at 441 nm, shown in the bottom panel. The differences are between O_{20} casts and B_1 (o; 1 m off the stern) or B_6 (×; 6 m off the stern) BBOP casts.

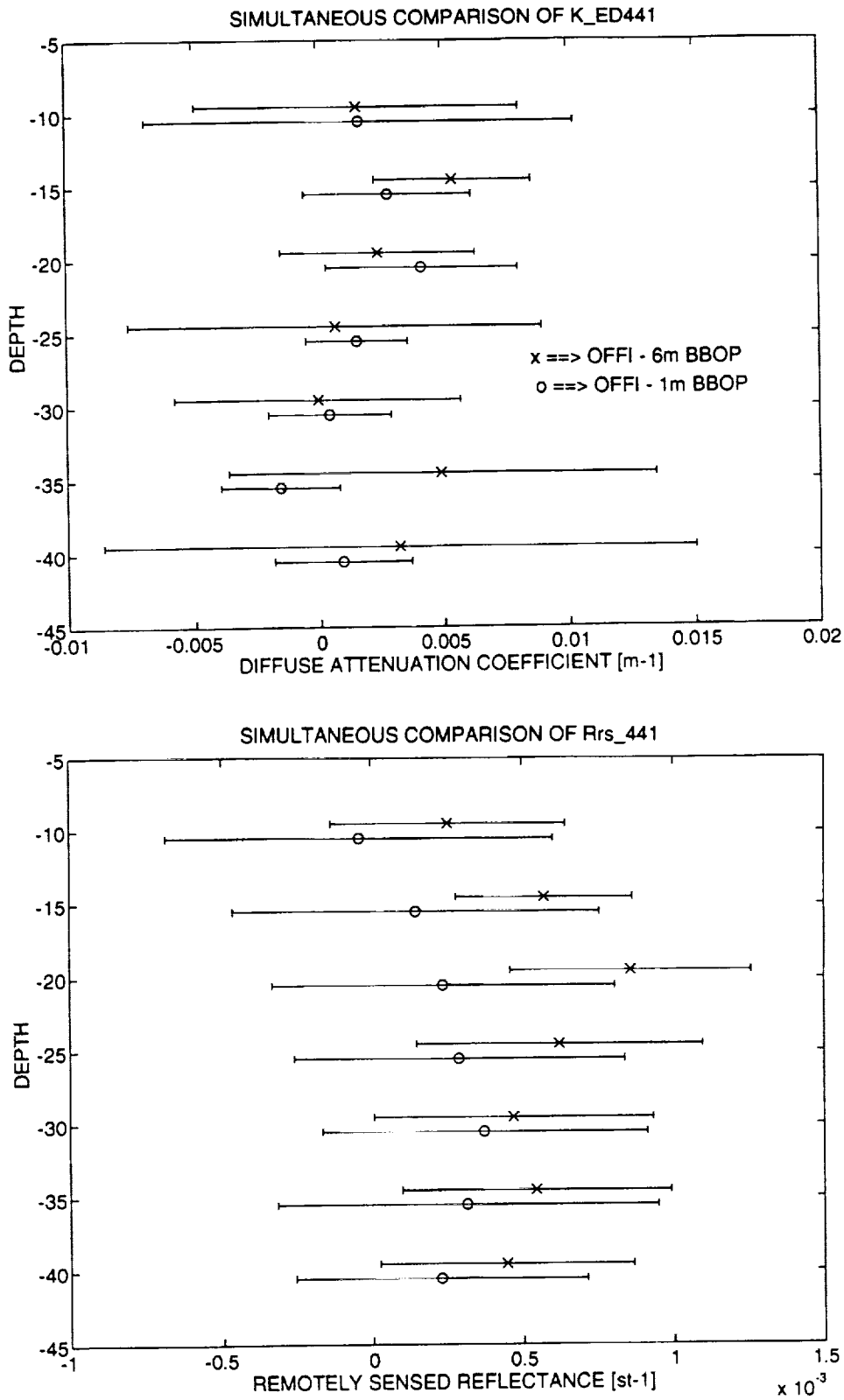

Fig. 15. Mean differences (with 90% c.i.) of simultaneous determinations of the diffuse attenuation coefficient for downwelling irradiance, $K_d(z, 441)$, shown in the top panel, and the remotely sensed reflectance, $R_{rs}(z, 441)$, shown in the bottom panel. The differences are between O_{20} casts and B_1 (o; 1 m off the stern) or B_6 (×; 6 m off the stern) BBOP casts.

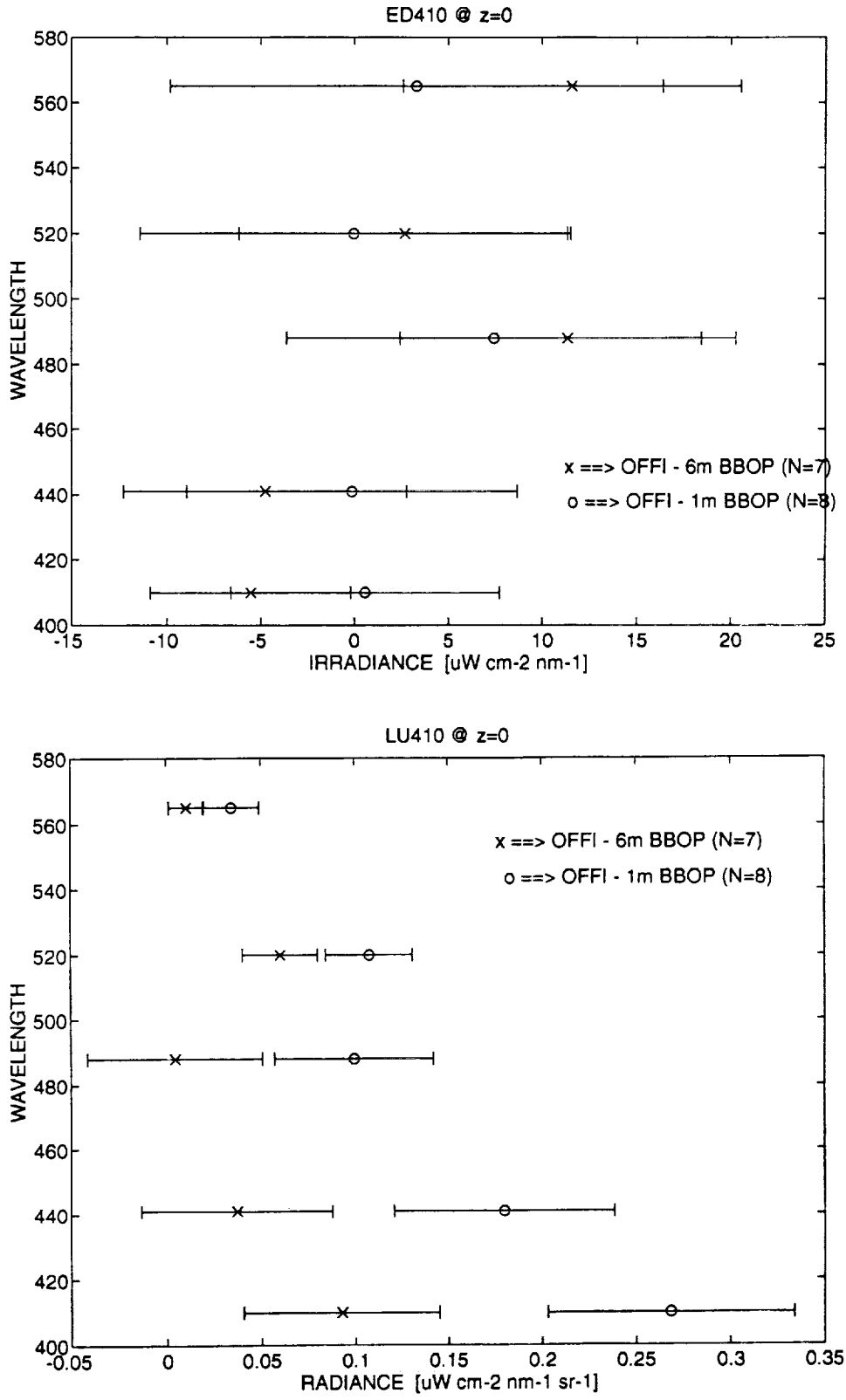

Fig. 16. Mean differences (with 90% c.i.) of simultaneous determinations of the downwelling irradiance spectrum just beneath the sea surface, $E_d(0^-, \lambda)$, shown in the top panel, and the upwelling radiance spectrum just beneath the sea surface, $L_u(0^-, \lambda)$, shown in the bottom panel. The differences are between O_{20} casts and B_1 (o; 1 m off the stern) or B_6 (×; 6 m off the stern) BBOP casts.

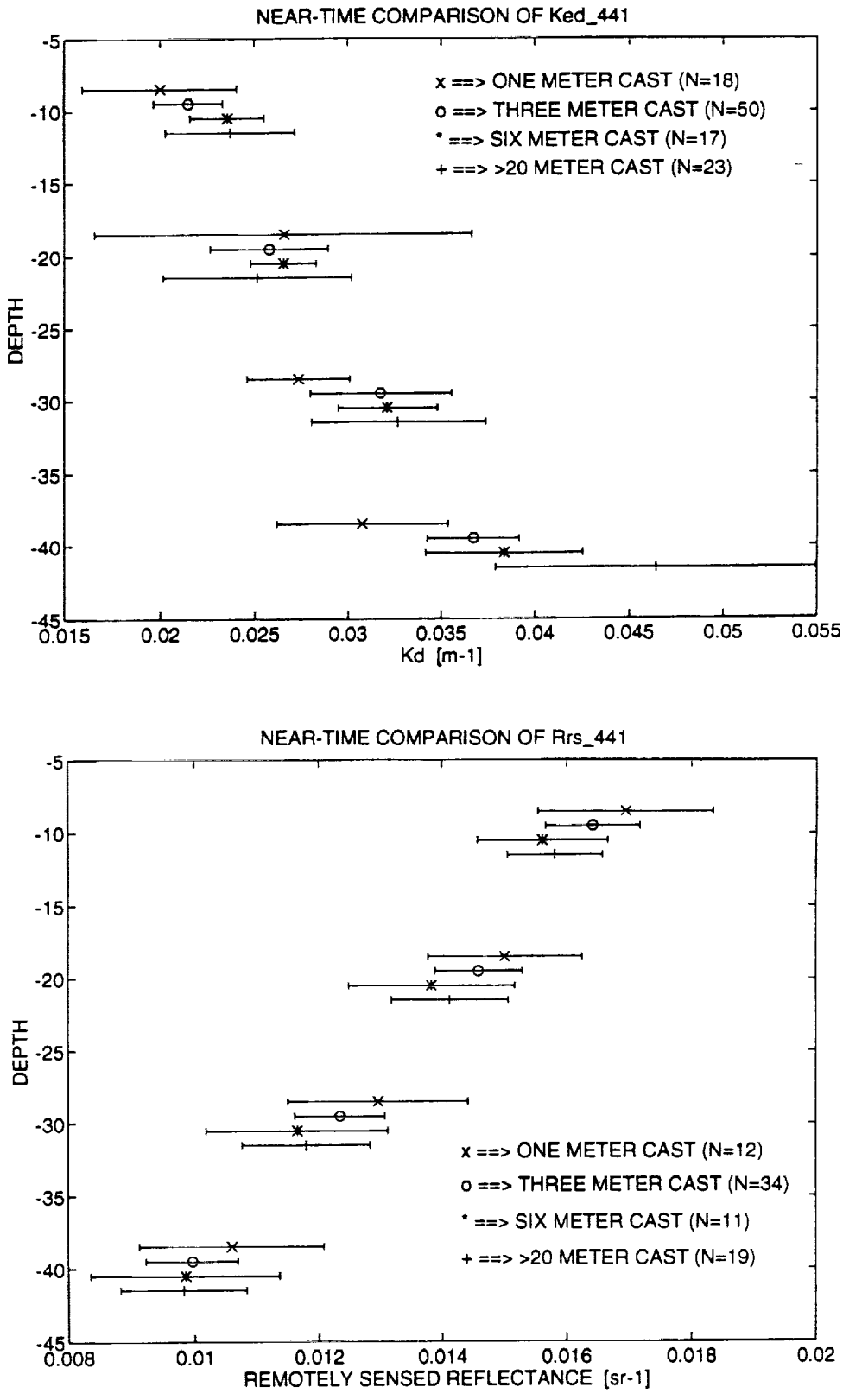

Fig. 17. Mean (with 90% c.i.) determinations of the diffuse attenuation coefficient for downwelling irradiance, $K_d(z, 441)$, shown in the top panel, and the remotely sensed reflectance, $R_{rs}(z, 441)$, shown in the bottom panel, as a function of depth for four different deployment distances (1, 3, 6, and > 20 m).

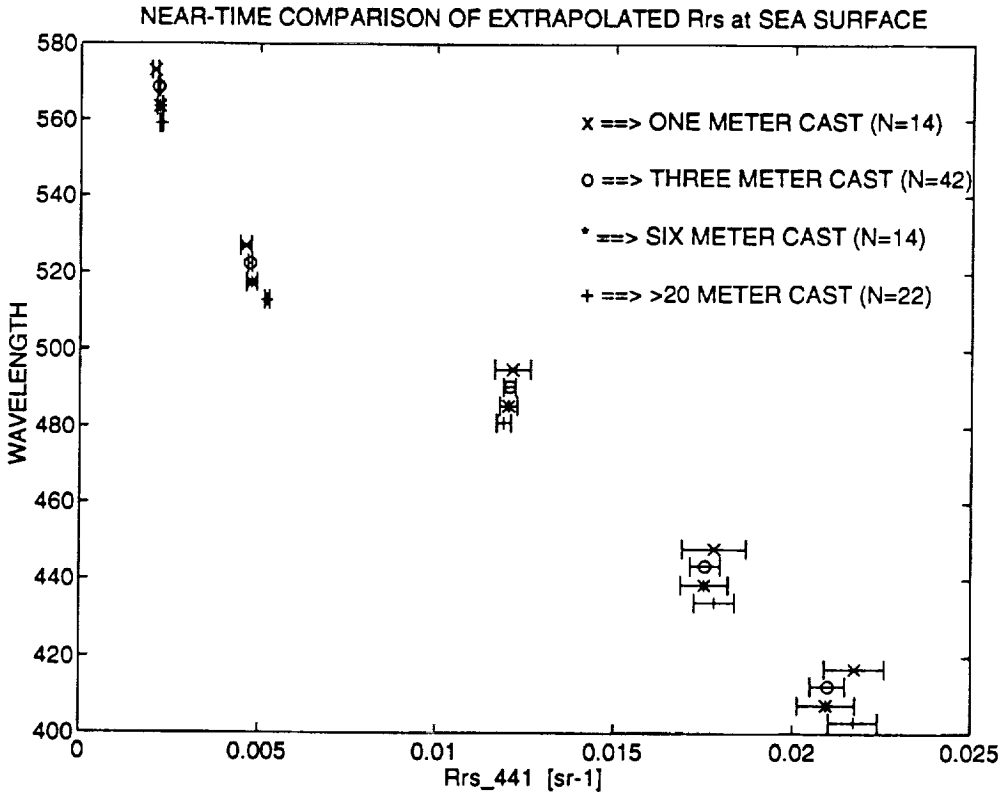

Fig. 18. Spectral structure of the remote sensing reflectance just beneath the sea surface, $R_{rs}(0^-, \lambda)$, evaluated at four different deployment distances (1, 3, 6, and greater than 20 m).

of geophysical and sampling noise. Voss et al. (1986) found very little differences (less than 6%) in values of $K_d(z, \lambda)$ and $R_{rs}(z, \lambda)$ profiles taken at 0 and 9 m from the ship. The differences were 0–3% and 1–6%, respectively, in the upper 20 m. Below 20 m, moreover, they found that the effects of the ship shadow have altogether disappeared, as is shown in this study.

In conclusion, little variability in downwelling irradiance is observed for any of the deployment distances off the *Weatherbird II*. Significant variations are found, however, for upwelling radiance when the deployment distance is less than 3 m. These findings suggest that the ship's shadow exerts its greatest influence in the upper 20 m, with the largest perturbation at the sea surface. Measurements of optical properties from the *Weatherbird II* during clear skies with the stern pointed into the sun can be made as long as the deployment distance off the stern is 3 m or greater. It is stressed that this analysis holds only for deployments made off the stern of the R/V *Weatherbird II* under clear sky conditions. The effects of variable sea state, sun glint, diffuse sky, and different hull shapes and sizes have not been evaluated, and additional experiments are necessary.

Acknowledgments

This work was supported by the National Science Foundation (OCE 91-16372 and OCE 90-16990), NASA (NAGW-3145), and the SeaWiFS Project Office. Computational support from Digital Equipment Corporation's flagship research project, Sequoia 2000, is also gratefully acknowledged.

Chapter 5

SeaWiFS Global Fields: What's In a Day?

GUILLERMO PODESTA
Rosenstiel School for Marine and Atmospheric Sciences
University of Miami
Miami, Florida

ABSTRACT

This chapter defines the procedure to be employed to delineate data corresponding to *one day* of SeaWiFS operation. The definition is required for data analysis with minimal temporal aliasing in the same region of observation. The definition also allows proper assignment of data into daily fields which will be used for the generation of weekly and monthly average products.

5.1 INTRODUCTION

The basic products to be generated by the SeaWiFS Project are global daily fields of geophysical quantities, such as phytoplankton pigment concentration. The daily fields will be the basis of subsequent temporal compositing into weekly and monthly products. One basic question, however, is: what constitutes a *day's worth* of data? This question is the subject of this chapter.

The need for a consistent definition of a *data day* is only truly relevant to the production or analysis of *global* data fields. If one is dealing with a limited area (although in this case, *limited* means anything less than global, and can encompass entire ocean basins), one takes advantage of the fact that satellite sensors usually sample a region at *approximately* the same time, or times, every day. In this way, data separated by approximately 24-hour periods can be assigned to different data days. Analyses of the resulting daily data fields will introduce a minimal amount of temporal aliasing, as the difference in sampling times will be on the order of a couple hours over an approximate repeat cycle of a few days.

In contrast, when daily global satellite data fields are to be constructed, a consistent definition of a data day needs to be adopted. This definition should be easy to implement in practice and should minimize temporal aliasing and discontinuities in the resulting products. In the following sections, some of the various alternatives will be explored.

5.2 TEMPORAL DEFINITION

The most obvious definition of a data day is a 24-hour period. For instance, a daily field would encompass all the data collected between 00:00:00 Coordinated Universal Time (UTC) (or any other arbitrary start of the day) and 23:59:59 UTC. This definition is simple, intuitive, and extremely easy to implement. Its negative aspects, however, will become apparent when one considers the orbital characteristics of the SeaStar spacecraft on which SeaWiFS will be flown.

To illustrate the problem, a plot of nadir tracks is presented for the SeaStar spacecraft (Fig. 19). To simplify the visualization, only the descending tracks are displayed, i.e., the spacecraft is flying from north to south. The SeaStar descending tracks correspond to daytime data, which is the only data archived for SeaWiFS other than special calibration measurements. The nadir tracks were generated using the program `SeaTrack`, made available by the SeaWiFS Project. A dummy set of orbital elements for the SeaStar spacecraft [in North American Air Defense (NORAD) Command two-line format] was also obtained from the Project.

For comparison with subsequent cases, the choice is to begin the hypothetical 24-hour data day on 2 April 1994 at 00:00:00 UTC, when the nadir track intersects the 180° meridian (marked Beg on Fig. 19). The descending orbit immediately after the beginning of the data day is labeled N. Subsequent descending tracks pass to the west, and are offset by a distance of about 25° of longitude at the equator. The swaths viewed by SeaWiFS in consecutive orbits have an increasingly larger overlap with latitude. This means that areas at high latitudes (greater than about 50°) may be sampled twice or more during a data day. When an area is sampled in two consecutive descending orbits, measurements will be separated by about an hour and a half. Unless one is concerned with features having

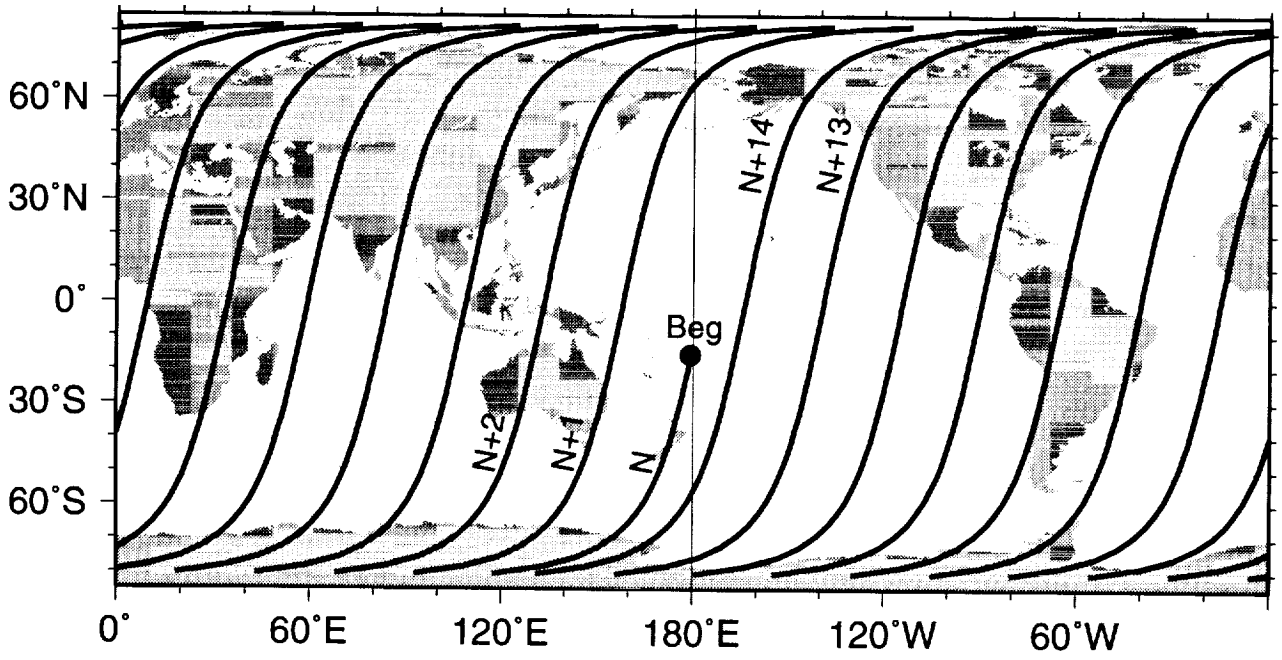

Fig. 19. Descending SeaStar tracks for a 24-hour data day beginning on 2 April 1994 00:00:00 UTC. The data day begins at the point labeled **Beg**. The day ends during an ascending orbit (not shown). The first orbit after the beginning of the data day is labeled N, and subsequent orbits are labeled N+1...N+14.

very small scales, or with calculation of rates, it is probably safe to assume that the ocean fields will not change significantly between consecutive passes; thus, temporal aliasing should be negligible. At the same time, at low and intermediate latitudes (approximately between 50° S and 50° N), the swaths do not overlap, and there will be gaps in the daily coverage (Hooker and Esaias 1993).

The SeaStar polar platform, which will carry SeaWiFS, is planned to have an orbital period of approximately 99 minutes. The actual period will depend on the spacecraft altitude, and therefore, may vary with time as the altitude of the satellite changes. Given an orbital period of about 99 minutes, the number of revolutions that the SeaStar spacecraft will complete in a 24-hour period is approximately 14.55. The last descending orbit of the 24-hour data day is labeled N+14. It is apparent from Fig. 19 that the 24-hour day leaves a large gap in coverage north of the beginning of the day, between orbits N+1 and N+14.

A second problem inherent in the temporal definition of a data day is the existence of areas on the global fields with large temporal discontinuities in sampling times, even though these areas may be spatially contiguous. For instance, consider descending track N+14 in Fig. 19, the last track of the data day. To the north of that track, i.e., over the Arctic Ocean north of Alaska, data are contributed by track N+1 and, possibly N+2, although this orbit appears to be too far north. These two tracks, however, were sampled near the beginning of the data day, more than 20 hours before track N+14. The daily fields will then contain, in addition to a wide gap, large temporal discontinuities between data swaths from tracks N+14 and N+1. If there is overlap between the two swaths, data collected far apart in time may be averaged, once again introducing potential aliasing. Similar problems occur in the area south of track N (south of New Zealand), which is sampled by tracks N+14 and N+13 much later in the day.

The large gaps in coverage, as well as potential aliasing and temporal discontinuity effects associated with the 24-hour definition, are further complicated by the fact that the locations where gaps occur change in time. Figure 20 shows the locations, along the SeaStar nadir tracks, of the boundaries between 24-hour data days for a 10-day period beginning on 2 April 1994. The dot labeled 1 corresponds to the beginning of the period on 2 April 1994 at 00:00:00 UTC. The dot labeled 2 indicates the beginning of the second 24-hour data day, and so forth. The dot marked 11 corresponds to the end of the period on 12 April 1994 at 00:00:00 UTC. The shift in the location of the daily boundaries is a direct result of the difference between the 24-hour data day and the longer time it would take the spacecraft to complete a number of revolutions which would ensure global coverage.

5.3 SPATIAL DEFINITION

Because of the problems associated with a temporal data day definition, the implications of adopting a spatial definition have been explored. In this case, the boundary between data days is not defined by time, but by a

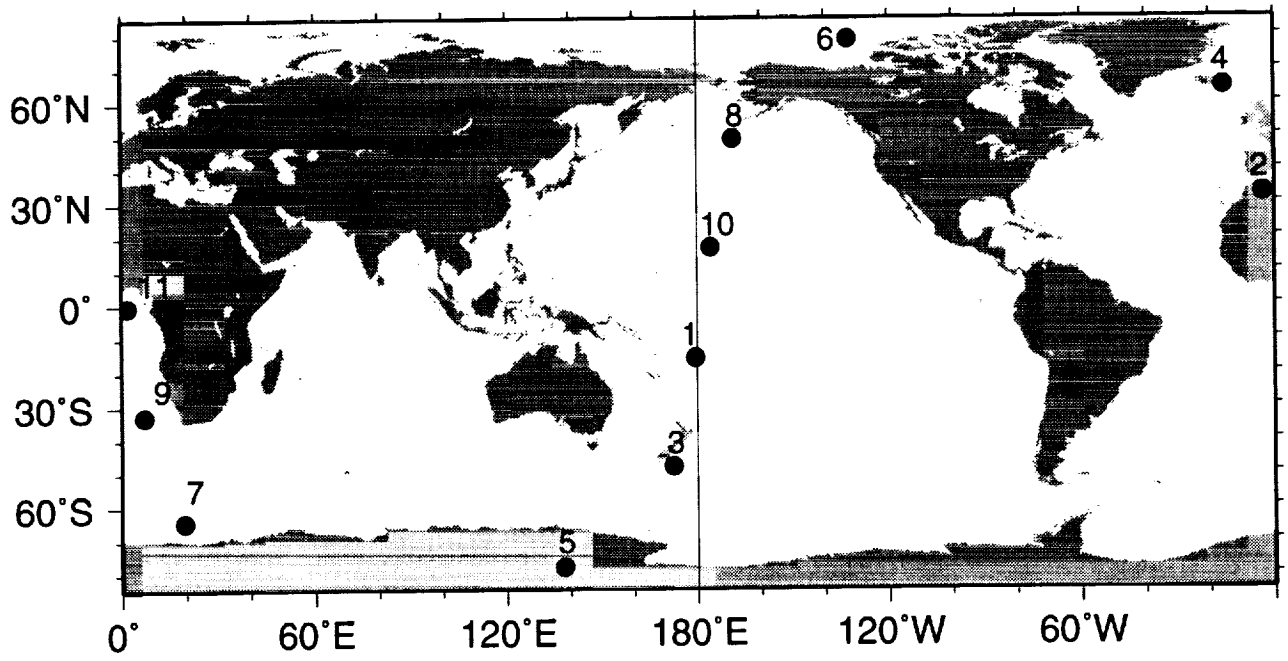

Fig. 20. Locations of the boundaries of 24-hour data days for a 10-day period beginning on 2 April 1994 00:00:00 UTC, at the dot labeled 1.

fixed geographic reference. A similar criterion is commonly used for designating orbit numbers in several spacecraft—the orbit number usually is incremented upon crossing the equator. For initial investigations, the 180° meridian was selected as the boundary between data days.

Figure 21 shows SeaStar nadir tracks for a spatially-defined data day. Because the nadir tracks cross the reference line seven or eight times during a day, one of the crossings must be selected to be the beginning of a data day. An operational definition for the selection of the crossing, which initiates the data day, is presented in Fig. 21. For this discussion, the day is defined to begin on 2 April 1994 at 00:00:00 UTC, when the spacecraft crosses the 180° meridian flying from north to south. Notice that this is the same time at which the 24-hour data day shown on Fig. 19 started, but it is entirely fortuitous that the 180° crossing took place at 00:00:00. The first descending track of the day is labeled N.

In this case, the end of the data day is defined as the moment when the nadir track crosses the 180° meridian during revolution N+15. This happens, for the example given, approximately on 3 April 1994 at 00:30:00 UTC. The observation most readily apparent is that a spatial definition will result in a data day that does not necessarily correspond to a 24-hour day; in this case, the data day is approximately 24 hours and 30 minutes long.

Note that Fig. 21 is approximate for two reasons. First, sometimes one less revolution is required to ensure almost complete global coverage, that is, the last orbit of the day would be N+14. The data day would be about 23 hours and 22 minutes long in this case. Second, the spatial definition is applied on a pixel-by-pixel basis, that is, pixels along the same scan line on a given orbit can be assigned to different days, depending on whether they are on one side or the other of the 180° meridian.

Figure 22 illustrates the pixel-by-pixel assignment of data to a given day. The figure shows a schematic description of the sampling pattern of the SeaWiFS instrument as it flies over the 180° meridian. Because there is not yet a scanner model for SeaWiFS, nadir tracks and scan lines are shown for the Advanced Very High Resolution Radiometer (AVHRR), which has slightly wider scans than SeaWiFS.

The figure shows about 20 minutes of nadir track, i.e., ±10 minutes from the 180° meridian crossing. The scan lines shown on Fig. 22 are separated by one minute. Pixels along a given scan line that are located east of 180° are assigned to day K (K is an arbitrary designation for a given day). If pixels along the same scan line are west of 180°, those pixels are assigned to the following day (K+1). It is apparent from Fig. 22 that even before the nadir track crosses the 180° meridian, pixels are already being assigned to day K+1. Conversely, after the nadir track has crossed the reference meridian, pixels east of the meridian are still being allocated to day K. It is this allocation mechanism that makes it difficult to precisely define the duration of a data day.

5.3.1 Beginning of the Data Day

How is the spatial definition of a data day implemented in routine processing of global satellite data fields? The first step is to define a meridian, which will serve as the

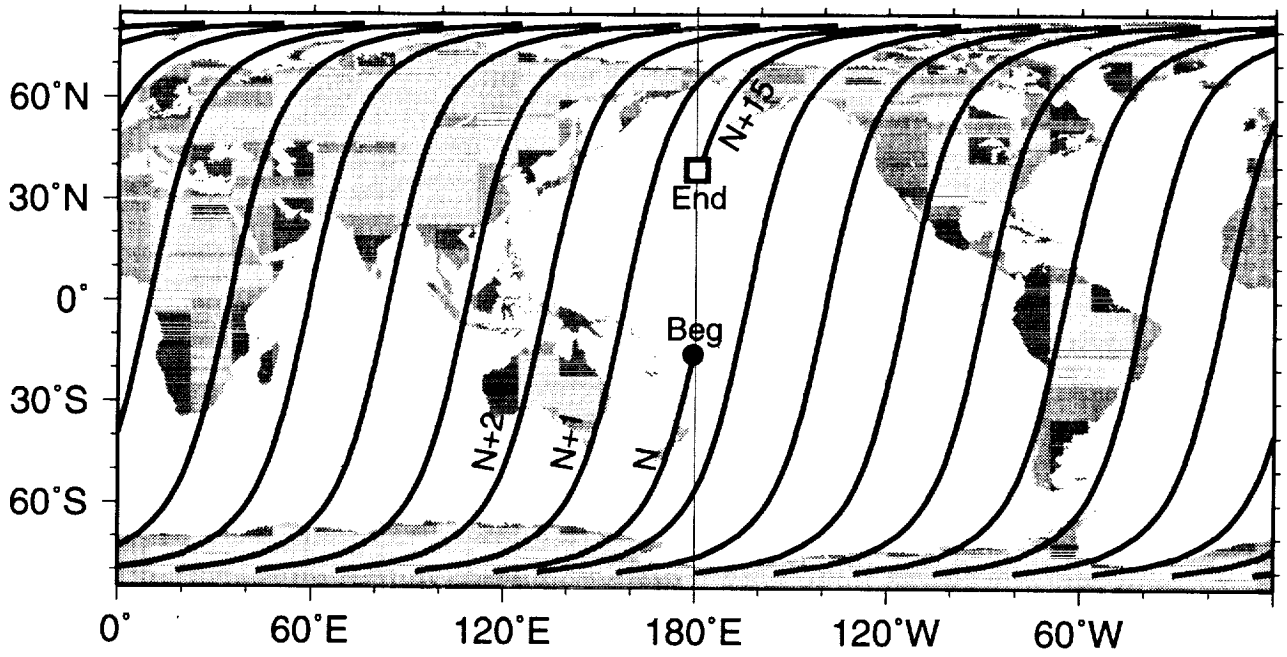

Fig. 21. SeaStar descending orbits for a spatially-defined data day beginning on 2 April 1994 00:00:00 UTC. At this time, the nadir track crosses the 180° meridian. The day ends when the nadir track crosses the 180° meridian (square labeled End) on 3 April 1994 00:30:00 UTC.

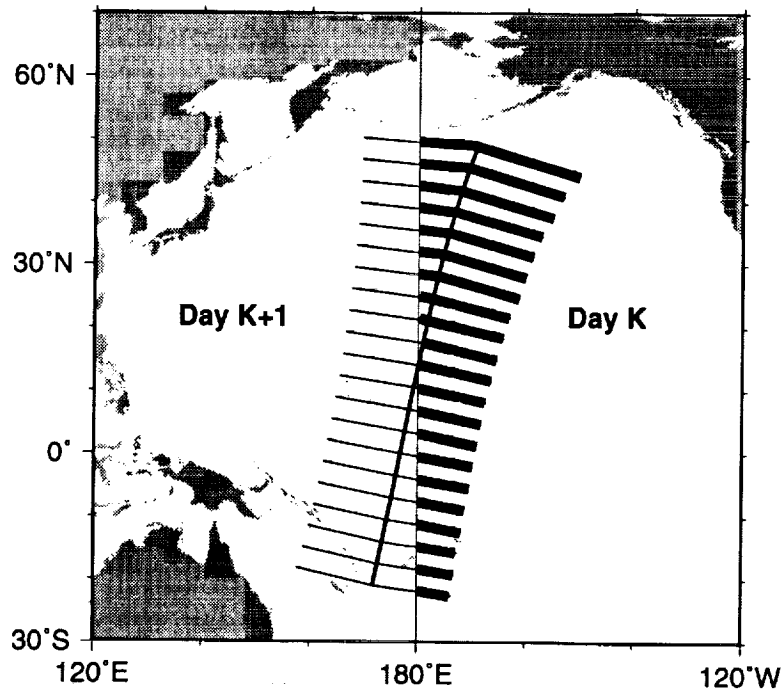

Fig. 22. AVHRR nadir track and scan lines for a 20 minute period centered about the 180° meridian crossing. Pixels to the east of the 180° meridian (marked in a thicker line) get assigned to a given data day K, whereas the pixels to the west of the meridian correspond to data day K+1.

reference for the spatial definition. The 180° meridian used in the previous examples is a good choice, as it minimizes differences between actual dates and the dates assigned to the data days. As the spatial data days are not 24 hours long, a suitable naming convention will have to be established.

A second step in defining a data day is to decide which of the descending crossings of the reference meridian will mark the beginning of each data day. As mentioned above, there are either seven or eight descending crossings of the reference meridian in a day. This pattern is illustrated in Fig. 23, which shows the latitude of descending crossings of the 180° meridian as a function of time for the SeaStar spacecraft, beginning on 2 April 1992 at 00:00:00 UTC. A period of about 10 days duration, ending on 12 April 1994 at 00:37:00 UTC, is shown in the figure. Most of the crossings (shown as dots) take place at high latitudes, and one or two crossings per day occur at tropical-to-intermediate latitudes.

For a given day, any of the crossings of the 180° meridian shown on Fig. 23 can be potentially selected as the one marking the beginning of a data day for descending orbits. For operational purposes, the following definition is proposed: *A data day for descending orbits is defined to begin at the descending crossing of the 180° meridian that is closest to the equator.* Crossings that satisfy this definition are shown as large squares in Fig. 23. Such a definition will be the easiest to implement because there is always only one crossing in a day that fulfills the condition. Consecutive crossings may, however, in certain instances have very similar absolute latitudes of intersection, one in the Southern Hemisphere, and the other in the Northern Hemisphere.

The alternating solid and dashed lines in Fig. 23 indicate consecutive data days. Initially, the latitude of data day initiation seems to follow a regular progression to the south, alternating between the Northern and Southern Hemispheres. Note, however, that the progression is interrupted near the end of the period illustrated. In this case, the next to last crossing would continue the progression, but the following crossing (the last square in the sequence) is actually closer to the equator. Following the proposed definition, the data day is extended until the next crossing, which is located in the Northern Hemisphere, i.e., the data day is slightly longer—one more revolution in this case. The southward progression of the crossings subsequently resumes.

Table 19 lists the start times of descending data days for a 15-day period beginning on 2 April 1994, as well as the latitude where the crossing of the 180° meridian occurs. It must be stressed that, because of the pixel-by-pixel allocation described above, parts of the field will include data collected both before and after the times listed in Table 19. In addition, as stated above, an appropriate naming convention will have to be worked out for the data days. For instance, the data day considered as *April 4* actually begins on 3 April 23:52 UTC and ends on 5 April 00:23 UTC.

Table 19. The beginning times of 15 data days for descending orbits of the SeaStar spacecraft. The latitude of the 180° meridian crossing is also shown.

Date [April 1994]	Beginning Time [UTC]	Latitude of 180° Crossing
2	00:00:00	−16.1
3	00:30:00	35.7
3	23:52:00	−22.9
5	00:23:00	27.4
5	23:46:00	−31.8
7	00:17:00	18.0
7	23:39:00	−39.5
9	00:11:00	7.8
9	23:32:00	−46.0
11	00:05:00	− 2.7
12	00:37:00	42.9
12	23:59:00	−13.0
13	23:52:00	−22.9
15	00:24:00	27.4
15	23:46:00	−31.7

5.3.2 Advantages of the Spatial Definition

In the previous sections, a spatial definition was proposed for a data day, together with an objective definition for the temporal *beginning* and *end* of such a data day. So far, however, the advantages or disadvantages of the proposed definitions have not been discussed.

Problems associated with the temporal definition of the data day were:

1) The potential presence of gaps,
2) Aliasing and large temporal discontinuities, and
3) The changing locations of the 24-hour data day boundaries.

The spatial definition avoids temporal changes in the location of boundaries, as the boundary is fixed, e.g., the 180° meridian. Furthermore, the spatial definition, to some extent, reduces gaps in the coverage. The presence of large temporal discontinuities among adjacent areas is still present, however.

The large temporal discontinuities identified on Fig. 19, north of Alaska and south of New Zealand, are still present in Fig. 21. It is clear that the large temporal discontinuities occur in two places near the meridian that define the separation between data days. The first place is the area south of the first track of the data day and west of the reference line. The second area with discontinuities occurs north of the last track of the data day, east of the reference line. As a result of the large temporal discontinuities that occur between adjacent swaths when the swaths overlap at higher latitudes, data that were sampled far apart in time will once again be averaged. Elsewhere on the global

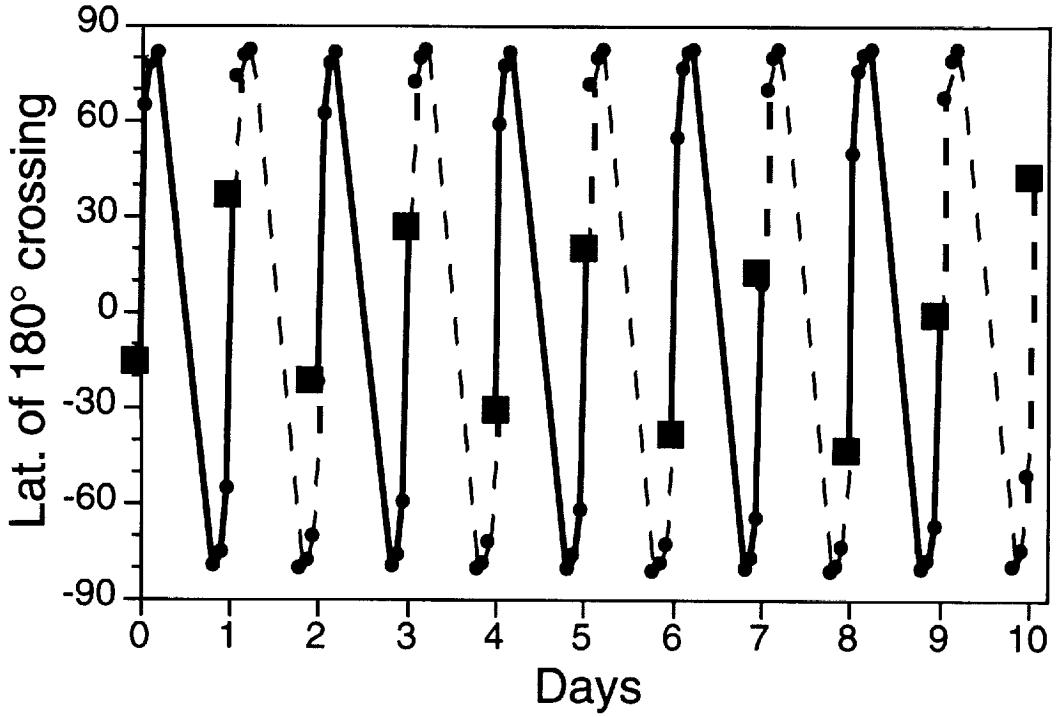

Fig. 23. Latitude of crossing of the 180° meridian for SeaStar descending orbits. The data shown are for a period approximately 10 days long, beginning on 2 April 1994 00:00:00 UTC and ending on 12 April 1994 00:37:00 UTC. Crossings are indicated by small dots. Large squares indicate crossings that begin data days. The alternating solid and dashed lines indicate consecutive data days.

fields, any given track is surrounded by tracks sampled one orbital period (about 99 minutes) earlier or later.

The presence of temporal discontinuities, or the averaging of data collected at very different times, may not be too important for some applications, although users should certainly be made aware of the occurrence of these events. In other situations, however, such temporal discontinuities may cause significant problems. Examples of such applications may be the estimation of the translation speed of certain features, or the computation of fluxes.

In order to limit the large meridional temporal discontinuities near the data day boundary, the short track segments north and south of the first and last tracks of the data day could simply be eliminated (e.g., parts of N+1, N+2, N+3, N+13, and N+14). This approach is illustrated in Fig. 24, which shows descending tracks between 2 April 1994 00:00:00 UTC and 3 April 1994 00:30:00 UTC, i.e., the data day shown on Fig. 21. The map is now centered at 0°, rather than at 180°, as in Fig. 21. Note that the nadir tracks, for which segments were eliminated, seem to end a bit before or after the 180° line. This break occurs because positions were predicted at one-minute increments by the orbital model used.

The elimination of segments may result in areas not being sampled, e.g., upper left and lower right corners of the map. These gaps might possibly be filled by the swath of the first and last tracks of the data day (tracks N and N+15 in the south and north, respectively). The size of the gaps is, however, a function of the latitude of the reference line crossing which defines the beginning of the data day. As shown in Fig. 23, this latitude changes with time, moving north and south approximately between 50° N and 50° S. When the crossing is farther north, the gap to the south of the first track will be larger. Conversely, when the crossing is further south, the gap north of the last track will get larger.

It is proposed that one additional swath be added at each end of the data day in order to replace the eliminated segments. Plots of nadir tracks for days in which the crossings are farthest north or south (not shown here) have shown that one additional swath is enough to fill each of the gaps, and a second swath would not make a significant contribution. The added swaths would be temporally continuous with the first and last tracks of each data day, thus eliminating the problems of temporal discontinuities. An operational scheme would involve the following steps:

1. The times corresponding to the beginning and end of a spatially-defined data day are found following the definition suggested above. These times will be referred to as the *beginning* and *end* of the data day.
2. Data east of the 180° meridian, collected up to 12 hours after the beginning of the data day,

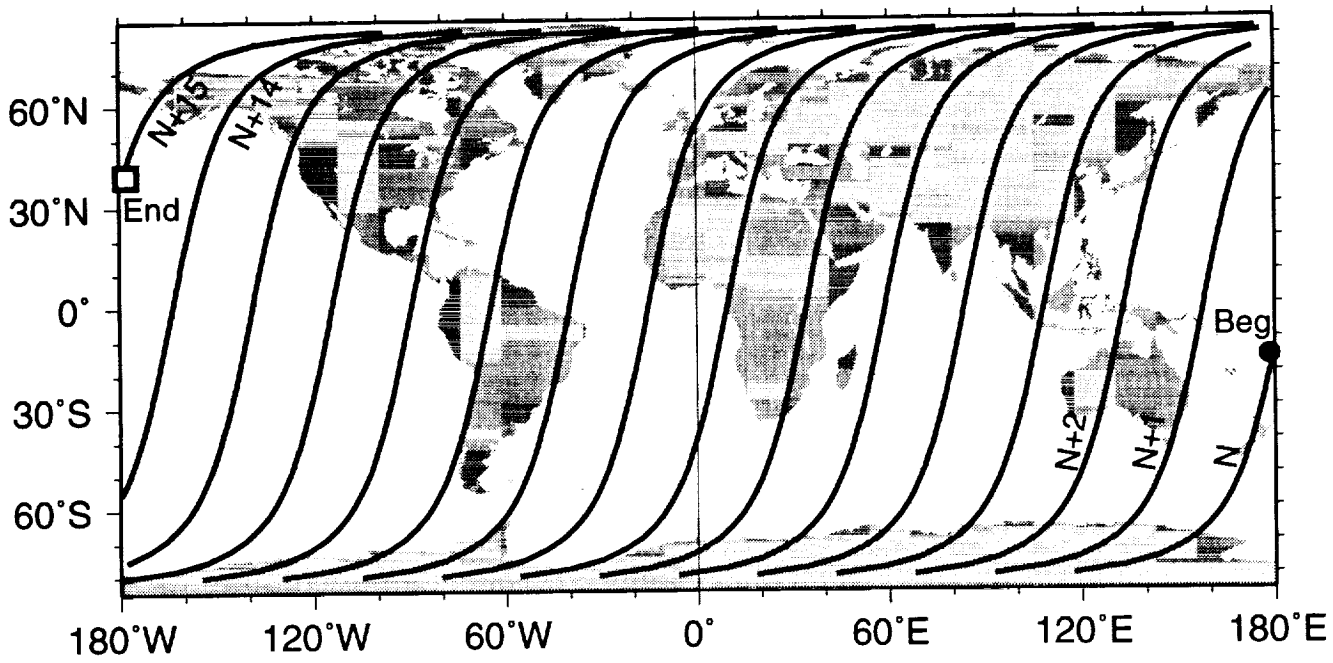

Fig. 24. SeaStar descending orbits for a spatially-defined data day beginning on 2 April 1994 00:00:00 UTC. Segments that introduce large north-south temporal discontinuities (see text) are excluded.

will be excluded. Data west of the 180° meridian, sampled up to 12 hours before the end of the data day, will be similarly excluded. The net result of these actions is similar to the elimination of segments shown in Fig. 24.

3. To ensure full coverage, data collected up to 99 minutes before the beginning of the data day, and covering the area west of the 180° meridian, will be added to the beginning of the data day. This addition fills the gap to the south of the first track of the day. Data collected up to 99 minutes after the end of the data day, sampling the area east of 180°, are also added. These data fill the gap north of the last track of the data day. The end result is illustrated in Fig. 25.

Figure 25 shows the descending orbits for the data day beginning approximately on 2 April 1994 00:00:00 UTC. The gaps shown in Fig. 24 have been filled by the addition of two short segments, indicated by arrows and dotted lines, on Fig. 25. Note that these segments have been sampled before (N-1) and after (N+16)—the times estimated for the beginning and end of this data day (see Table 19). However, because the added segments are close in time to orbits N and N+15, the large temporal discontinuities have been eliminated. The segments excluded from this data day are the first portion of tracks N+1, N+2, and N+3 east of 180°, and the last portion of tracks N+13 and N+14 west of 180°.

5.3.3 An Alternative Explanation

To facilitate comprehension of the methodology, a simple analogy may be helpful. Envision a continuous strip chart on which the continents are drawn. Above the chart recorder there is a clock showing UTC time and date. As the chart moves from left to right, a pen draws descending tracks one at a time. The speed of the chart movement is appropriate to ensure that the nadir track's latitude and longitude, corresponding to any given UTC time, are correct, i.e., the nadir tracks should look similar to those on Figs. 24 and 25.

Suppose the chart is positioned so that the pen is just crossing the 180° meridian, near the equator, on 2 April 1994. The clock time should be about 00:00:00 UTC. The chart recorder is then allowed to run for almost 24 hours, until a track crosses the 180° meridian again at about 36° N. The time should be about 00:30:00 UTC on 3 April 1994. If the chart is cut along the two 180° meridians drawn (left and right), the tracks on the chart should look exactly like Fig. 24. As in Fig. 24, there will be some gaps in the coverage. On the right side of the chart, there is a gap south of the first track (N) of the day. This gap should have been filled by the last portion of tracks N+13 and N+14, which have been drawn to the left of the 180° meridian on the left side of the chart. These lines, however, were eliminated when the chart was cut along the left 180° line. Similarly, the gap north of the last track of the day should have been filled by the initial portions of tracks

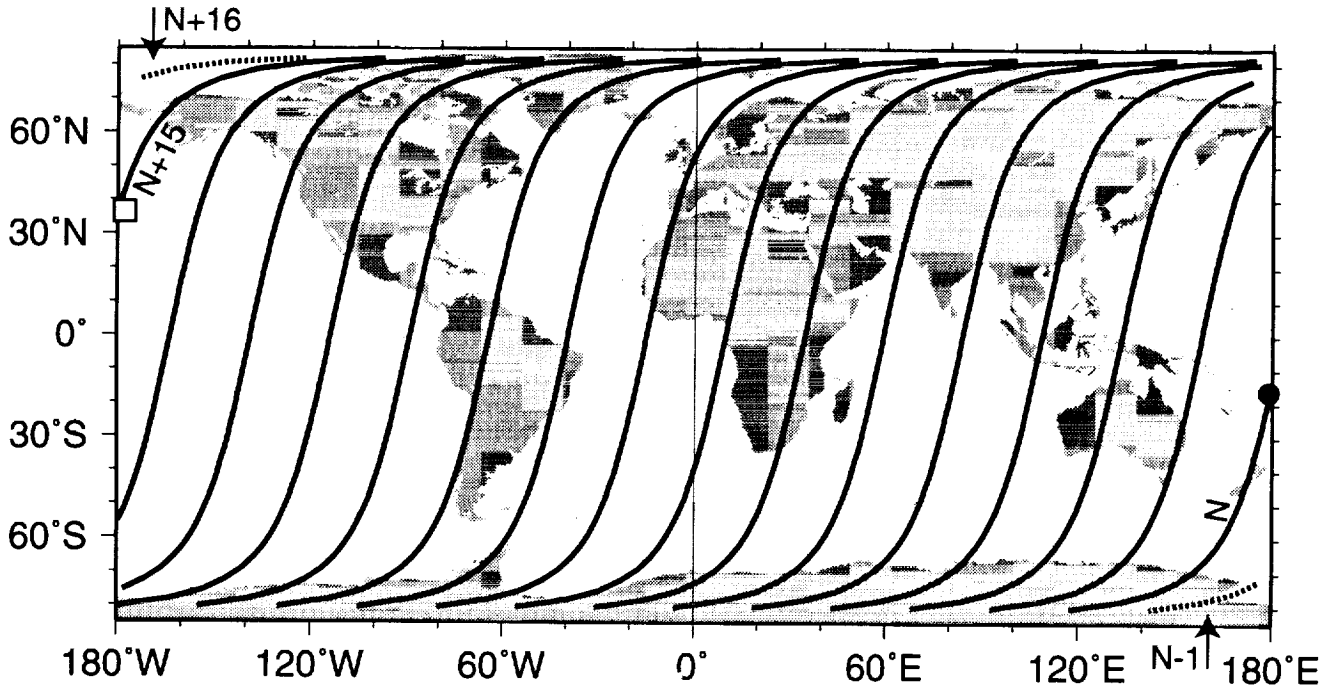

Fig. 25. The data day beginning on 2 April 1994 00:00:00 UTC, showing the addition of two segments (indicated by arrows and dotted lines) in order to minimize temporal discontinuities. The first track sampled after the estimated beginning time of the day (Beg) is track N. The added segment south of this track corresponds to the previous orbit (N-1). The last track before the estimated end time of the data day (End) is track N+15. The added segment to the north corresponds to the next orbit (N+16).

N+1, N+2 and N+3. These segments were drawn east of the 180° meridian on the right side of the plot. As the 180° line was cut along on the right, however, these segments were excluded. It is apparent that the chart recorder analogy reproduces the action of eliminating tracks which cause large temporal discontinuities, as the end result looks exactly like Fig. 24. The gaps can be filled in the global fields using the same chart recorder analogy.

Now envision the case in which the chart recorder does not start at 00:00:00 UTC on 2 April 1994, but rather, the chart is moved backwards and is started about 99 minutes earlier. If the recorder starts then, an additional track (N-1) will be drawn before the nadir track of orbit N crosses the 180° meridian at 00:00:00 UTC, which defines the temporal beginning of the data day. The southern portion of track N-1 will fall west of the 180° meridian, filling the gap previously existing in the south. Then the recorder is allowed to run up to 99 minutes past the time originally defined as the end of the day (3 April 1994, 00:30:00 UTC), and again, an additional track will be drawn. If the last track of the day is N+15, the northern portion of track N+16 will fill the northern gap. Once the recorder has been allowed to run for the estimated duration of the data day, plus the additional 99 minutes on either end, a pair of scissors is used to cut the chart along both 180° meridians. By doing this, the spatial pixel-by-pixel assignment of data is applied to a given data day. The end result should look exactly like Fig. 25. Finally, envision running the recorder for long periods and repeatedly cutting the long chart along the 180° meridians. Each of the maps would correspond to one data day.

When discussing an elimination of orbital segments that would result in large temporal discontinuities, the presentation could have given the impression that data in these segments would be unused, and therefore wasted. If the analogy presented above is followed, however, it is easy to see that the data will not be deleted, but rather the data will be assigned to the previous, or the following, data days. For instance, the northern portions of tracks N+1, N+2, and N+3 (not labeled) in Fig. 24 would be plotted to the east of the right 180° meridian on the chart. When the chart is cut, these portions get assigned to the previous data day, which begins on 1 April 1994 UTC. In the same way, the southernmost portions of tracks N+13 and N+14 are plotted to the west of the left 180° meridian; thus, being assigned to the next data day after the chart is cut along the meridian. The end result of the scheme proposed is a daily global field where all parts of a field are temporally separated from adjacent areas by, at most, one orbital period.

5.4 OTHER ISSUES

An aspect that has not been discussed so far is that at both the extreme north and extreme south of the fields, data from several tracks might be averaged within a data day. At high latitudes, the spacecraft is flying in nearly an east-west direction and, thus, the scan lines have a north-south orientation. For instance, there are five or six passes a day at high latitudes (Fig. 23) near the 180° meridian. Some of these passes are excluded at high latitudes, as described above. In other high latitude regions, however, the fields will contain the average of several passes. This overlap should not have too many consequences on SeaWiFS products, as the areas affected will be mostly on land in the Southern Hemisphere and under permanent ice cover in the Northern Hemisphere. Furthermore, in these regions the sensor may encounter limitations in available sunlight, which may preclude sampling.

One final issue requiring discussion is that the spatial scheme proposed above will result in temporal discontinuities in areas that straddle the reference line. Suppose that a study is made of an area of the North Pacific Ocean, encompassed between 150° W and 150° E, and straddling the 180° line. If this study obtains a global field for a given data day, it must be realized that the portion of the study area west of 180° has been sampled much earlier than the portion to the east. Again, this may not be relevant for some research, but it could be in some cases. A solution would be to place the reference line elsewhere, e.g., along 0°, but there will always be some location where areas on either side of the line will be sampled far apart in time. Alternatively, a user might obtain product fields for two consecutive data days and paste the appropriate portions. In the Pacific example presented above, the eastern part of the study area would be extracted from data day K and the western part from day K+1.

To study the *daily* data of a region that includes 180° longitude, two consecutive daily products should be joined at the seam. This procedure will produce data that are continuous across the 180° meridian. These daily scenes can then be averaged over time using a time binning algorithm to construct weekly or longer period composites of an area straddling the 180° meridian. This method would produce the most accurate long-term composites. One could, however, use the standard global products by joining areas east and west of 180° from the same weekly, monthly, or annual product. The latter method will result in a slight temporal discontinuity across the 180° meridian, since the earliest data contributing to the composite west of 180° is not matched by continuous data east of 180°. Similarly, data east of 180° is not matched by data west of 180° on the final day of the composite.

GLOSSARY

A-band Absorption Band
AOP Apparent Optical Properties
AVHRR Advanced Very High Resolution Radiometer

BATS Bermuda Atlantic Time-Series Study
BBOP Bermuda Bio-Optics Project
BRDF Bidirectional Reflectance Distribution Function
BSI Biospherical Instruments, Inc.

CHORS Center for Hydro-Optics and Remote Sensing
c.i. confidence interval
CVT Calibration and Validation Team
CZCS Coastal Zone Color Scanner

DC Digital Count

EOSDIS Earth Observing System Data Information System

FEL Not an acronym; designates a type of irradiance lamp.

GSFC Goddard Space Flight Center

IFOV Instantaneous Field-of-View

JGOFS Joint Global Ocean Flux Study

MER Marine Environmental Radiometer

NASA National Aeronautics and Space Administration
NIST National Institute of Standards and Technology
NORAD North American Air Defense (Command)

OFFI Optical Free-Falling Instrument

PST Pacific Standard Time

R/V Research Vessel

SBRC Santa Barbara Research Center
SDSU San Diego State University
SeaWiFS Sea-viewing Wide Field-of-view Sensor
SI International System of Units (*Systéme International d' Unités*)
SIS Spherical Integrating Source
S/N Serial Number
SNR Signal-to-Noise Ratio
SPIE Society of Photo-Optical Instrumentation Engineers

TOA Top of the Atmosphere

UCSB University of California at Santa Barbara
UTC Coordinated Universal Time

SYMBOLS

a Regression coefficient.

b Regression coefficient.
B Band 7 width.
B_1 BBOP casts 1 m from the ship's stern.
B_6 BBOP casts 6 m from the ship's stern.

$c(\lambda)$ Spectral beam attenuation coefficient.

E_d Incident downwelling irradiance.
$E_d(z,\lambda)$ Downwelled spectral irradiance.
E_u Incident upwelling irradiance.
$E_u(z,\lambda)$ Upwelled spectral irradiance.

$f(\lambda)$ Instrument spectral response function.
F_i Immersion coefficient.

k Molecular absorption cross-section area.
$K_d(z,\lambda)$ Vertical attenuation coefficient for downwelling irradiance.
$K_L(z,\lambda)$ Vertical attenuation coefficient for upwelled radiance.
$K_u(z,\lambda)$ Vertical attenuation coefficient for upwelled irradiance.

L Radiance of light transmitted through absorbing oxygen.
L_t Radiance measured at a satellite, i.e., orbiting sensor.
L_0 Model radiance without absorbing oxygen.
L_{atm} Radiance of light reflected from the atmosphere.
L_{sfc} Radiance of light leaving an ocean surface and passing through the atmosphere.
$L_u(z,\lambda)$ Upwelled spectral radiance.

m Air mass.

N Total number of oxygen molecules per unit area in a vertical column of the atmosphere.

O_{20} OFFI casts 20 m from the ship's stern.
p Surface pressure.
p_{dev} Pressure deviation between the minimum and maximum surface pressures compared to 1,013 mb.
p_{ref} Reference pressure.

R^2 The square of the linear correlation coefficient.
$R_{rs}(z,\lambda)$ Remote sensing reflectance.

$S(\lambda)$ Solar spectral irradiance.
s_{xy} Residual standard deviation.

$T(\lambda)$ Two-way transmission through oxygen in the model layer.
$T(\lambda,\theta,\theta_0)$ Two-way transmission through oxygen in the model layer in terms of zenith angle (θ), and solar angle (θ_0).

W Equivalent bandwidth.

ΔL The difference between L and L_0.
Δp The difference in atmospheric pressure.

θ Zenith angle of the line-of-sight in a plane-parallel atmosphere.
θ_0 Solar zenith angle.

λ Wavelength.

ρ Reflectance.

σ Standard deviation.

$\tau_{\text{ox}}(\lambda)$ Optical thickness due to oxygen absorption.

ξ Actual deployment distance.
ξ_d Calculated deployment distance for downwelling irradiance measurements.
ξ_u Calculated deployment distance for upwelling irradiance measurements.
ξ_L Calculated deployment distance for upwelling radiance measurements.

χ Proportionality constant.

References

Barnes, R.A., 1994: *SeaWiFS Data: Actual and Simulated.* [World Wide Web page.] From URLs: `http://seawifs.gsfc.nasa.gov/SEAWIFS/IMAGES/spectra1.dat` and `/spectra2.dat` NASA Goddard Space Flight Center, Greenbelt, Maryland.

——, A.W. Holmes, W.L. Barnes, W.E. Esaias, C.R. McClain, and T. Svitek, 1994: SeaWiFS Prelaunch Radiometric Calibration and Spectral Characterization. *NASA Tech. Memo. 104566, Vol. 23,* S.B. Hooker, E.R. Firestone, and J.G. Acker, Eds., NASA Goddard Space Flight Center, Greenbelt, Maryland, 55 pp.

Biggar, S.F., D.I. Gellman, and P.N. Slater, 1990: Improved optical depth components from Langley plot data. *Remote Sens. Environ.,* **32,** 91–101.

——, P.N. Slater, K.J. Thome, A.W. Holmes, and R.A. Barnes, 1993: Preflight solar-based calibration of SeaWiFS. *SPIE,* **1,939,** 233–242.

Cantor, A.J., and A.E. Cole, 1985: *Handbook of Geophysics and the Space Environment,* A.S. Jursa, Ed., Air Force Geophysics Laboratory, Air Force Systems Command, USAF, 15–48.

Clark, D.K., 1981: Phytoplankton pigment algorithms for the Nimbus-7 CZCS. In: *Oceanography from Space,* J.F.R. Gower, Ed., Plenum Press, New York, 227–237.

Dickey, T.D., and D.A. Siegel, 1993: Bio-Optics in U.S. JGOFS. *U.S. JGOFS Planning Report Number 18,* U.S. JGOFS Planning and Coordination Office, Woods Hole, Massachusetts, 180 pp.

Ding, K., and H.R. Gordon, 1994: Analysis of the influence of O_2 "A" band absorption on atmospheric correction of ocean color imagery. *Appl. Opt.,* (submitted).

Gordon, H.R., 1985: Ship perturbation of irradiance measurements at sea. 1: Monte Carlo simulations. *Appl. Opt.,* **24,** 4,172–4,182.

——, and D.K. Clark, 1980: Atmospheric effects in the remote sensing of phytoplankton pigments. *Bound.-Layer Meterol.,* **18,** 299–313.

Helliwell, W.S., G.N. Sullivan, B. Macdonald, and K.J. Voss, 1990: Ship shadowing: model and data comparisons. *Ocean Optics X,* R.W. Spinrad, Ed., *SPIE,* **1,302,** 55–71.

Hooker, S.B., W.E. Esaias, G.C. Feldman, W.W. Gregg, and C.R. McClain, 1992: An Overview of SeaWiFS and Ocean Color. *NASA Tech. Memo. 104566, Vol. 1,* NASA Goddard Space Flight Center, Greenbelt, Maryland, 24 pp., plus color plates.

——, and ——, 1993: An overview of the SeaWiFS Project. *EOS, Trans. AGU,* **74,** 241.

McClain, C.R., W.E. Esaias, W. Barnes, B. Guenther, D. Endres, S. Hooker, G. Mitchell, and R. Barnes, 1992: Calibration and Validation Plan for SeaWiFS. *NASA Tech. Memo. 104566, Vol. 3,* S.B. Hooker and E.R. Firestone, Eds., NASA Goddard Space Flight Center, Greenbelt, Maryland, 41 pp.

——, J.C. Comiso, R.S. Fraser, J.K. Firestone, B.D. Schieber, E. Yeh, K.R. Arrigo, and C.W. Sullivan, 1994: Case Studies for SeaWiFS Calibration and Validation, Part 1. *NASA Tech. Memo. 104566, Vol. 13,* S.B. Hooker and E.R. Firestone, Eds., NASA Goddard Space Flight Center, Greenbelt, Maryland, 52 pp., plus color plates.

Mueller, J.L., 1994: Preliminary Comparison of Irradiance Immersion Coefficients for Several Marine Environmental Radiometers (MERs). *CHORS Tech. Memo. 004-94,* Center for Hydro-Optics and Remote Sensing, San Diego State University, San Diego, California, 4 pp.

——, and R.W. Austin, 1992: Ocean Optics Protocols for SeaWiFS Validation. *NASA Tech. Memo. 104566, Vol. 5,* S.B. Hooker and E.R. Firestone, Eds., NASA Goddard Space Flight Center, Greenbelt, Maryland, 45 pp.

——, and R.W. Austin, 1995: Ocean Optics Protocols for SeaWiFS Validation, Revision 1. *NASA Tech. Memo. 104566, Vol. 25,* S.B. Hooker, E.R. Firestone, and J.G. Acker, Eds., NASA Goddard Space Flight Center, Greenbelt, Maryland, 69 pp.

Neckel, H., and D. Labs, 1984: The solar radiation between 3,300 and 12,500 Å. *Solar Phys.,* **90,** 205–258.

Poole, H.H., 1936: The photo-electric measurement of submarine illumination in offshore waters. *Rapp. Proc-Verb. Conseil Expl. Mar.,* **101,** 9.

Siegel, D.A., A.F. Michaels, J. Sorensen, M. Hammer, and M.C. O'Brien, 1994: Seasonal variability of light availability and its utilization in the Sargasso Sea. *J. Geophys. Res.,* (submitted).

Sorensen, J.C., M. O'Brien, D. Konoff, and D.A. Siegel, 1994: The BBOP data processing system. *Ocean Optics XII,* J.S. Jaffe, Ed., *SPIE,* **2,258,** 539–546.

Strickland, J.D.H., 1958: Solar radiation penetrating the ocean: A review of requirements, data, and methods of measurement, with particular reference to photosynthetic productivity. *J. Fish. Res. Bd. Canada,* **15,** 453–493.

Voss, K.J., J.W. Nolten, and G.D. Edwards, 1986: Ship shadow effects on apparent optical properties. *Ocean Optics VIII,* P.N. Slater, Ed., *SPIE,* **637,** 186–190.

United States Navy, 1978: *Marine Climatic Atlas of the World; South Atlantic Ocean, Vol. 4,* NAVAIR 50-1C-531, US Government Printing Office, Washington, DC, 325 pp.

Waters, K.J., R.C. Smith, and M.R. Lewis, 1990: Avoiding ship induced light-field perturbation in the determination of oceanic optical properties. *Oceanogr.,* **3,** 18–21.

Weir, C.T., D.A. Siegel, D.W. Menzies, and A.F. Michaels, 1994: *In situ* evaluation of a ship's shadow. *Ocean Optics XII,* J.S. Jaffe, Ed., *SPIE,* **2,258,** 815–821.

Wu, M.C., 1985: Remote sensing of cloud-top pressure using reflected solar radiation in the oxygen A-band. *J. Climate Appl. Meteorol.,* **24,** 540–546.

THE SEAWIFS TECHNICAL REPORT SERIES

Vol. 1

Hooker, S.B., W.E. Esaias, G.C. Feldman, W.W. Gregg, and C.R. McClain, 1992: An Overview of SeaWiFS and Ocean Color. *NASA Tech. Memo. 104566, Vol. 1,* S.B. Hooker and E.R. Firestone, Eds., NASA Goddard Space Flight Center, Greenbelt, Maryland, 24 pp., plus color plates.

Vol. 2

Gregg, W.W., 1992: Analysis of Orbit Selection for SeaWiFS: Ascending vs. Descending Node. *NASA Tech. Memo. 104566, Vol. 2,* S.B. Hooker and E.R. Firestone, Eds., NASA Goddard Space Flight Center, Greenbelt, Maryland, 16 pp.

Vol. 3

McClain, C.R., W.E. Esaias, W. Barnes, B. Guenther, D. Endres, S. Hooker, G. Mitchell, and R. Barnes, 1992: Calibration and Validation Plan for SeaWiFS. *NASA Tech. Memo. 104566, Vol. 3,* S.B. Hooker and E.R. Firestone, Eds., NASA Goddard Space Flight Center, Greenbelt, Maryland, 41 pp.

Vol. 4

McClain, C.R., E. Yeh, and G. Fu, 1992: An Analysis of GAC Sampling Algorithms: A Case Study. *NASA Tech. Memo. 104566, Vol. 4,* S.B. Hooker and E.R. Firestone, Eds., NASA Goddard Space Flight Center, Greenbelt, Maryland, 22 pp., plus color plates.

Vol. 5

Mueller, J.L., and R.W. Austin, 1992: Ocean Optics Protocols for SeaWiFS Validation. *NASA Tech. Memo. 104566, Vol. 5,* S.B. Hooker and E.R. Firestone, Eds., NASA Goddard Space Flight Center, Greenbelt, Maryland, 43 pp.

Vol. 6

Firestone, E.R., and S.B. Hooker, 1992: SeaWiFS Technical Report Series Summary Index: Volumes 1–5. *NASA Tech. Memo. 104566, Vol. 6,* S.B. Hooker and E.R. Firestone, Eds., NASA Goddard Space Flight Center, Greenbelt, Maryland, 9 pp.

Vol. 7

Darzi, M., 1992: Cloud Screening for Polar Orbiting Visible and IR Satellite Sensors. *NASA Tech. Memo. 104566, Vol. 7,* S.B. Hooker and E.R. Firestone, Eds., NASA Goddard Space Flight Center, Greenbelt, Maryland, 7 pp.

Vol. 8

Hooker, S.B., W.E. Esaias, and L.A. Rexrode, 1993: Proceedings of the First SeaWiFS Science Team Meeting. *NASA Tech. Memo. 104566, Vol. 8,* S.B. Hooker and E.R. Firestone, Eds., NASA Goddard Space Flight Center, Greenbelt, Maryland, 61 pp.

Vol. 9

Gregg, W.W., F.C. Chen, A.L. Mezaache, J.D. Chen, J.A. Whiting, 1993: The Simulated SeaWiFS Data Set, Version 1. *NASA Tech. Memo. 104566, Vol. 9,* S.B. Hooker, E.R. Firestone, and A.W. Indest, Eds., NASA Goddard Space Flight Center, Greenbelt, Maryland, 17 pp.

Vol. 10

Woodward, R.H., R.A. Barnes, C.R. McClain, W.E. Esaias, W.L. Barnes, and A.T. Mecherikunnel, 1993: Modeling of the SeaWiFS Solar and Lunar Observations. *NASA Tech. Memo. 104566, Vol. 10,* S.B. Hooker and E.R. Firestone, Eds., NASA Goddard Space Flight Center, Greenbelt, Maryland, 26 pp.

Vol. 11

Patt, F.S., C.M. Hoisington, W.W. Gregg, and P.L. Coronado, 1993: Analysis of Selected Orbit Propagation Models for the SeaWiFS Mission. *NASA Tech. Memo. 104566, Vol. 11,* S.B. Hooker, E.R. Firestone, and A.W. Indest, Eds., NASA Goddard Space Flight Center, Greenbelt, Maryland, 16 pp.

Vol. 12

Firestone, E.R., and S.B. Hooker, 1993: SeaWiFS Technical Report Series Summary Index: Volumes 1–11. *NASA Tech. Memo. 104566, Vol. 12,* S.B. Hooker and E.R. Firestone, Eds., NASA Goddard Space Flight Center, Greenbelt, Maryland, 28 pp.

Vol. 13

McClain, C.R., K.R. Arrigo, J. Comiso, R. Fraser, M. Darzi, J.K. Firestone, B. Schieber, E-n. Yeh, and C.W. Sullivan, 1994: Case Studies for SeaWiFS Calibration and Validation, Part 1. *NASA Tech. Memo. 104566, Vol. 13,* S.B. Hooker and E.R. Firestone, Eds., NASA Goddard Space Flight Center, Greenbelt, Maryland, 52 pp., plus color plates.

Vol. 14

Mueller, J.L., 1993: The First SeaWiFS Intercalibration Round-Robin Experiment, SIRREX-1, July 1992. *NASA Tech. Memo. 104566, Vol. 14,* S.B. Hooker and E.R. Firestone, Eds., NASA Goddard Space Flight Center, Greenbelt, Maryland, 60 pp.

Vol. 15

Gregg, W.W., F.S. Patt, and R.H. Woodward, 1994: The Simulated SeaWiFS Data Set, Version 2. *NASA Tech. Memo. 104566, Vol. 15,* S.B. Hooker and E.R. Firestone, Eds., NASA Goddard Space Flight Center, Greenbelt, Maryland, 42 pp., plus color plates.

Vol. 16

Mueller, J.L., B.C. Johnson, C.L. Cromer, J.W. Cooper, J.T. McLean, S.B. Hooker, and T.L. Westphal, 1994: The Second SeaWiFS Intercalibration Round-Robin Experiment, SIRREX-2, June 1993. *NASA Tech. Memo. 104566, Vol. 16,* S.B. Hooker and E.R. Firestone, Eds., NASA Goddard Space Flight Center, Greenbelt, Maryland, 121 pp.

Vol. 17

Abbott, M.R., O.B. Brown, H.R. Gordon, K.L. Carder, R.E. Evans, F.E. Muller-Karger, and W.E. Esaias, 1994: Ocean Color in the 21st Century: A Strategy for a 20-Year Time Series. *NASA Tech. Memo. 104566, Vol. 17,* S.B. Hooker and E.R. Firestone, Eds., NASA Goddard Space Flight Center, Greenbelt, Maryland, 20 pp.

Vol. 18

Firestone, E.R., and S.B. Hooker, 1994: SeaWiFS Technical Report Series Summary Index: Volumes 1–17. *NASA Tech. Memo. 104566, Vol. 18,* S.B. Hooker and E.R. Firestone, Eds., NASA Goddard Space Flight Center, Greenbelt, Maryland, 47 pp.

Vol. 19

McClain, C.R., R.S. Fraser, J.T. McLean, M. Darzi, J.K. Firestone, F.S. Patt, B.D. Schieber, R.H. Woodward, E-n. Yeh, S. Mattoo, S.F. Biggar, P.N. Slater, K.J. Thome, A.W. Holmes, R.A. Barnes, and K.J. Voss, 1994: Case Studies for SeaWiFS Calibration and Validation, Part 2. *NASA Tech. Memo. 104566, Vol. 19,* S.B. Hooker, E.R. Firestone, and J.G. Acker, Eds., NASA Goddard Space Flight Center, Greenbelt, Maryland, 73 pp.

Vol. 20

Hooker, S.B., C.R. McClain, J.K. Firestone, T.L. Westphal, E-n. Yeh, and Y. Ge, 1994: The SeaWiFS Bio-Optical Archive and Storage System (SeaBASS), Part 1. *NASA Tech. Memo. 104566, Vol. 20,* S.B. Hooker and E.R. Firestone, Eds., NASA Goddard Space Flight Center, Greenbelt, Maryland, 40 pp.

Vol. 21

Acker, J.G., 1994: The Heritage of SeaWiFS: A Retrospective on the CZCS NIMBUS Experiment Team (NET) Program. *NASA Tech. Memo. 104566, Vol. 21,* S.B. Hooker and E.R. Firestone, Eds., NASA Goddard Space Flight Center, Greenbelt, Maryland, 43 pp.

Vol. 22

Barnes, R.A., W.L. Barnes, W.E. Esaias, and C.R. McClain, 1994: Prelaunch Acceptance Report for the SeaWiFS Radiometer. *NASA Tech. Memo. 104566, Vol. 22,* S.B. Hooker, E.R. Firestone, and J.G. Acker, Eds., NASA Goddard Space Flight Center, Greenbelt, Maryland, 32 pp.

Vol. 23

Barnes, R.A., A.W. Holmes, W.L. Barnes, W.E. Esaias, C.R. McClain, and T. Svitek, 1994: SeaWiFS Prelaunch Radiometric Calibration and Spectral Characterization. *NASA Tech. Memo. 104566, Vol. 23,* S.B. Hooker, E.R. Firestone, and J.G. Acker, Eds., NASA Goddard Space Flight Center, Greenbelt, Maryland, 55 pp.

Vol. 24

Firestone, E.R., and S.B. Hooker, 1995: SeaWiFS Technical Report Series Summary Index: Volumes 1–23. *NASA Tech. Memo. 104566, Vol. 24,* S.B. Hooker and E.R. Firestone, Eds., NASA Goddard Space Flight Center, Greenbelt, Maryland, (in press).

Vol. 25

Mueller, J.L., and R.W. Austin, 1995: Ocean Optics Protocols for SeaWiFS Validation, Revision 1. *NASA Tech. Memo. 104566, Vol. 25,* S.B. Hooker and E.R. Firestone, Eds., NASA Goddard Space Flight Center, Greenbelt, Maryland, 67 pp.

Vol. 26

Siegel, D.A., M.C. O'Brien, J.C. Sorensen, D.A. Konnoff, E.A. Brody, J.L. Mueller, C.O. Davis, W.J. Rhea, and S.B. Hooker, 1995: Results of the SeaWiFS Data Analysis Round-Robin (DARR), July 1994. *NASA Tech. Memo. 104566, Vol. 26,* S.B. Hooker and E.R. Firestone, Eds., NASA Goddard Space Flight Center, Greenbelt, Maryland, 58 pp.

Vol. 27

J.L. Mueller, R.S. Fraser, S.F. Biggar, K.J. Thome, P.N. Slater, A.W. Holmes, R.A. Barnes, C.T. Weir, D.A. Siegel, D.W. Menzies, A.F. Michaels, and G. Podesta 1995: Case Studies for SeaWiFS Calibration and Validation, Part 3. *NASA Tech. Memo. 104566, Vol. 27,* S.B. Hooker, E.R. Firestone, and J.G. Acker, Eds., NASA Goddard Space Flight Center, Greenbelt, Maryland, 46 pp.

REPORT DOCUMENTATION PAGE

Form Approved
OMB No. 0704-0188

1. AGENCY USE ONLY *(Leave blank)*	2. REPORT DATE	3. REPORT TYPE AND DATES COVERED
	May 1995	Technical Memorandum

4. TITLE AND SUBTITLE
SeaWiFS Technical Report Series
Volume 27-Case Studies for SeaWiFS Calibration and Validation, Part 3

5. FUNDING NUMBERS
Code 970.2

6. AUTHOR(S) James L. Mueller, Robert S. Fraser, Stuart F. Biggar, Kurtis J. Thome, Philip N. Slater, Alan W. Holmes, Robert A. Barnes, Christian T. Weir, David A. Siegel, David W. Menzies, Anthony F. Michaels, and Guillermo Podesta
Series Editors: Stanford B. Hooker and Elaine R. Firestone
Technical Editor: James G. Acker

7. PERFORMING ORGANIZATION NAME(S) AND ADDRESS(ES)
Laboratory for Hydrospheric Processes
Goddard Space Flight Center
Greenbelt, Maryland 20771

8. PERFORMING ORGANIZATION REPORT NUMBER
95B00084

9. SPONSORING/MONITORING AGENCY NAME(S) AND ADDRESS(ES)
National Aeronautics and Space Administration
Washington, D.C. 20546–0001

10. SPONSORING/MONITORING AGENCY REPORT NUMBER
TM–104566, Vol. 27

11. SUPPLEMENTARY NOTES James L. Mueller: San Diego State University, San Diego, California; Stuart F. Biggar, Kurtis J. Thome, and Philip N. Slater: University of Arizona, Tucson, Arizona; Alan W. Holmes: Santa Barbara Research Center, Santa Barbara, California; Robert A. Barnes: ManTech Environmental Technology, Inc., Wallops Island, Virginia; Christian T. Weir, David A. Siegel, and David W. Menzies: University of California at Santa Barbara, Santa Barbara, California; Anthony F. Michaels: Bermuda Biological Station for Research, Ferry Reach, Bermuda; Guillermo Podesta: University of Miami, Miami, Florida; Elaine R. Firestone: General Sciences Corporation, Laurel, Maryland; and James G. Acker: Hughes STX, Lanham, Maryland

12a. DISTRIBUTION/AVAILABILITY STATEMENT
Unclassified–Unlimited
Subject Category 48
Report is available from the Center for AeroSpace Information (CASI),
800 Elkridge Landing Road, Linthicum Heights, MD 21090; (301) 621-0390.

12b. DISTRIBUTION CODE

13. ABSTRACT *(Maximum 200 words)*

This document provides brief reports, or case studies, on a number of investigations sponsored by the Calibration and Validation Team (CVT) within the Sea-viewing Wide Field-of-view Sensor (SeaWiFS) Project. Chapter 1 describes a comparison of the irradiance immersion coefficients determined for several different marine environmental radiometers (MERs). Chapter 2 presents an analysis of how light absorption by atmospheric oxygen will influence the radiance measurements in band 7 of the SeaWiFS instrument. Chapter 3 gives the results of the second ground-based solar calibration of the instrument, which was undertaken after the sensor was modified to reduce the effects of internal stray light. (The first ground-based solar calibration of SeaWiFS is described in Volume 19 in the *SeaWiFS Technical Report Series.*) Chapter 4 evaluates the effects of ship shadow on subsurface irradiance and radiance measurements deployed from the deck of the R/V *Weatherbird II* in the Atlantic Ocean near Bermuda. Chapter 5 illustrates the various ways in which a single data day of SeaWiFS observations can be defined, and why the spatial definition is superior to the temporal definition for operational usage.

14. SUBJECT TERMS
SeaWiFS, Oceanography, Immersion Coefficients, MER, Band 7 Radiance, Solar Radiation, Ship Shadow, Data Day, Global Fields, Case Studies

15. NUMBER OF PAGES
46

16. PRICE CODE

17. SECURITY CLASSIFICATION OF REPORT	18. SECURITY CLASSIFICATION OF THIS PAGE	19. SECURITY CLASSIFICATION OF ABSTRACT	20. LIMITATION OF ABSTRACT
Unclassified	Unclassified	Unclassified	Unlimited